Chemical Engineering Science 240 (2021) 116655

Contents lists available at ScienceDirect

Chemical Engineering Science

journal homepage: www.elsevier.com/locate/ces

Particle-scale study of heat and mass transfer in a bubbling fluidised bed

Shuai Wang, Yansong Shen *

School of Chemical Engineering, University of New South Wales, Sydney, NSW 2052, Australia

HIGHLIGHTS

- Heat and mass transfer behaviours of char combustion are studied at a particle scale.
- Polydisperse drag model has to be used to accurately reproduce bed hydrodynamics.
- Axial dispersion coefficient is one order of magnitude larger than horizontal one.
- For reactive particles, the radiation and heat of reaction are dominated.
- For inert particles, the radiation and convection are dominated simultaneously.
- Particle concentration shows a weak influence on Nu_p and Sh_p.

GRAPHICAL ABSTRACT

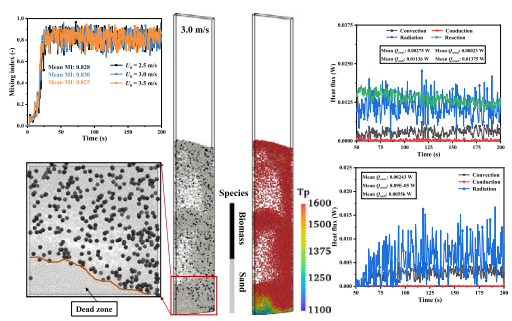

ARTICLE INFO

Article history:
Received 5 February 2021
Received in revised form 27 March 2021
Accepted 9 April 2021
Available online 20 April 2021

Keywords:
CFD-DEM
Heat and mass transfer
Char combustion
Bubbling fluidised bed
Mixing and dispersion

ABSTRACT

In this study, the multiphase flow and thermochemical behaviours of char combustion in a bubbling fluidised bed (BFB) are simulated using CFD-DEM approach featuring particle size polydispersity and thermochemical sub-models. The model is first validated in terms of mixing index, particle temperature, and particle diameter. Then, it is applied to examine the contribution of each heat transfer mode and study particle-scale behaviours of char and sand comprehensively. The results show that the polydisperse drag model should be used to accurately reproduce bed hydrodynamics when simulating a BFB system with polydisperse particles. Under the simulation conditions, the particle-averaged heat fluxes to char particles through convection, conduction, radiation, and char reaction take 9.79%, 0.82%, 40.44%, and 48.95%, respectively; the particle-averaged heat fluxes to sand particles through convection, conduction, and radiation take 30.28%, 1.0%, and 68.72%, respectively. For reactive char particles, the radiation and heat of reaction are dominated, while for inert sand particles, the radiation and convection are dominated; and for both particle species, the conduction is negligible. Axial dispersion coefficient is one order of magnitude larger than the horizontal one, demonstrating the dominant role of the introduced gas flow in determining bed hydrodynamics.

© 2021 Elsevier Ltd. All rights reserved.

1. Introduction

Solid fuel combustion in fluidised beds has been widely practised in many thermochemical conversion processes of fossil/renewable fuels (Zhong et al., 2016) and many manufacturing processes (Shen et al., 2014, 2016; Shen and Yu, 2016). Among all combustors, bubbling fluidised bed (BFB) is regarded as one of the most popular reactors due to its advantages of excellent solid mixing, easy temperature control, wide fuel flexibility, and low pollutant emission (Zhong et al., 2016). Also, the particles in these processes may vary and polydispersity may affect the thermo-

* Corresponding author.
E-mail address: ys.shen@unsw.edu.au (Y. Shen).

https://doi.org/10.1016/j.ces.2021.116655
0009-2509/© 2021 Elsevier Ltd. All rights reserved.

Nomenclature

$A_{p,i}$	Surface area of particle i, m^2
C_D	Drag coefficient
$C_{p,g}$	Specific heat capacity of gas phase, $J \cdot kg^{-1} \cdot K^{-1}$
$C_{p,i}$	Specific heat capacity of particle i, $J \cdot kg^{-1} \cdot K^{-1}$
D_n	Diffusion coefficient of species n, $kg \cdot m^{-1} \cdot s^{-1}$
d	Thickness of gas layer, m
d_p	Particle diameter, m
$e_{n,ij}$	Normal restitution coefficient
$\mathbf{F}_c$	Contact force exerting on a specific particle, N
$\mathbf{F}_d$	Gas force exerting on a specific particle, N
$\mathbf{F}_{ij}^n$, $\mathbf{F}_{ij}^t$	Normal and tangential contact forces between particle i and j, N
$\mathbf{g}$	Gravitational acceleration, $m \cdot s^{-2}$
$h_{pg,i}$	Convective heat transfer coefficient, $W \cdot m^{-2} \cdot K^{-1}$
$\mathbf{I}_{gm}$	Inter-phase momentum exchange rate, $N \cdot m^{-3}$
I_p	Moment of inertia of a specific particle, $kg \cdot m^2$
k	The number of particles colliding with particle i
k_f, k_a, k_r	Film resistance, ash layer resistance, surface reaction resistance
$k_{n,ij}$, $k_{t,ij}$	Normal and tangential spring coefficients, $N \cdot m^{-1}$
L	Distance from contact point to particle center, m
l_{ij}	Distance between particle i and j, m
L_x, L_y, L_z	Dimension of the bed along x ,y, and z directions
m_p, m_{eff}	Particle mass and effective particle mass, kg
MW_g	Molar weight of gas phase, $kg \cdot kmol^{-1}$
$\mathbf{n}_{ij}$	Normal unit vector between particle i and j
N_g	Number of gaseous species
N_p	Particle number
$N_{p,\Omega}$	Particle number in the domain Ω
$Nu_{p,i}$	Nusselt number of particle i
N_x, N_y, N_z	Grid number along x ,y, and z directions
P_g	Pressure of gas phase, Pa
P_{O_2}	Partial pressure of oxygen, atm
Pr	Prandtl number
Q_{gp}	Gas-particle convective heat transfer rate, $W \cdot m^{-3}$
Q_{pgp}	Particle-gas-particle conductive heat transfer rate, $W \cdot m^{-3}$
Q_{pp}	Particle-particle conductive heat transfer rate, $W \cdot m^{-3}$
Q_{rad}	Radiative heat transfer rate, $W \cdot m^{-3}$
r_d	Ratio of core diameter to particle diameter
R_g	Gas constant, $J \cdot mol^{-1} \cdot K^{-1}$
$R_{c,ij}$	Radius of contact region, m
Re_p	Particle Reynold number
R_{gn}	Mass source term due to chemical reactions of gas phase, $kg \cdot m^{-3} \cdot s^{-1}$
R_{sn}	Mass source term due to chemical reactions of solid phase, $kg \cdot m^{-3} \cdot s^{-1}$
R_{in}, R_{out}	Lower and upper bounds of conductive heat transfer region, m
$R_{p,i}$, $R_{p,j}$	Diameters of particle i and j, m
Sc	Schmidt number
S_g	Stress tensor of gas phase, Pa
Sh	Sherwood number
t	Time instant, s
$t_{n,ij}^{col}$	Collision time, s
$\mathbf{t}_{ij}$	Tangential unit vector between particle i and j
T_{env}	Temperature of environment, K
T_g	Temperature of gas phase, K
$T_{g,\Omega}$	Temperature of gas phase in the domain Ω, K
$T_{p,i}$, $T_{p,j}$	Temperatures of particle i and j, K
T_{Rg}	Radiation temperature of gas phase, K
$\mathbf{u}_g$	Velocity vector of gas phase, $m \cdot s^{-1}$
U_g	Gas velocity, $m \cdot s^{-1}$
$\mathbf{v}_p$	Velocity vector of particle i, $m \cdot s^{-1}$
υ_1	Stoichiometric coefficient
V_c	Volume of computational cell, m^3
V_i	Volume of particle i, m^3
X_n	Mass fraction of nth species

Greek symbols

ε_g	Void fraction
$\varepsilon_{p,i}$	Emissivity of particle i
β	Inter-phase momentum exchange coefficient, $kg \cdot m^{-3} \cdot s^{-1}$
ΔH_{rg}	Heat source of gas phase due to chemical reaction, $W \cdot m^{-3}$
ΔH_{rs}	Heat source of solid phase due to chemical reaction, $W \cdot m^{-3}$
κ_g	Thermal conductivity of gas, $W \cdot m^{-1} \cdot K^{-1}$
$\kappa_{p,i}$, $\kappa_{p,j}$	Thermal conductivity of particle i and j, $W \cdot m^{-1} \cdot K^{-1}$
γ_{Rg}	Radiative heat transfer coefficient of gas phase, $W \cdot m^{-2} \cdot K^{-4}$
$\eta_{n,ij}$, $\eta_{t,ij}$	Normal and tangential damping coefficients, $kg \cdot s^{-1}$
$\delta_{n,ij}$, $\delta_{t,ij}$	Normal and tangential overlap displacements, m
μ	Friction coefficient
μ_g	Gas viscosity, $kg \cdot m^{-1} \cdot s^{-1}$
ρ_g, ρ_p	Gas and particle density, $kg \cdot m^{-3}$
$\boldsymbol{\omega}_p$	Particle angular velocity, s^{-1}

Subscripts

g	Gas phase
i	Particle i
ij	Interactions between particle i and j
j	Particle j
n	Variables in normal direction
p	Properties of particle

Acronyms

BFB	Bubbling fluidised bed
CFD	Computational fluid dynamics
CFL	Coutant-Friedrich-Lewy
DEM	Discrete element method
FVM	Finite volume method
KTGF	Kinetic theory of granular flow
LSD	Linear spring dashpot
MFIX	Multiphase Flow with Interphase eXchange
UDF	User-defined function
3D	Three-dimensional

chemical behaviour and reactor performance. The BFB performance highly relies on the thermochemical behaviours of solid particles and gas-solid interactions (Zhou et al., 2004a, 2004b). Hence, for optimal design and optimisation of BFBs to achieve maximum efficiency, it is essential to explore the multiphase flow and thermochemical characteristics of dense gas-solid reacting flows in BFBs, especially when polydispersity affects.

So far, many experiments have been conducted and various correlations have been established to describe the hydrodynamics, heat, and mass transfer behaviours on both microscopic and macroscopic views (Botterill, 1975; Bu et al., 2015; Hayhurst and Parmar, 2002; Kunii and Levenspiel, 2013; Wakao and Kagei, 1982). Taking heat transfer for example, the temperature is usually measured by thermocouples. Based on the experimental data, one

can determine the total heat transfer coefficient of a specific particle. The experimental study is useful for researchers to correlate the operating parameters with the heat transfer coefficient but has limitations in unveiling the fundamentals. It is accepted that four heat transfer modes exist during the solid fuel combustion process, i.e., convection, conduction, radiation, and heat of reaction. However, experimental studies cannot quantify each heat transfer mode's contribution. Moreover, the thermochemical behaviours of solid fuel are highly influenced by the local gas-solid structures (e.g., sand inhibitory effect, bubble evolution) both in spatial and temporal scales (Hayhurst and Parmar, 2002; Medrano et al., 2017), which are very challenging for experimental measurements. In general, the experimental studies are costly and cannot provide an entirely internal state of thermochemical behaviours.

Recently, numerical simulation has been increasingly accepted as an alternative to studying the thermochemical characteristics of dense gas-solid reacting flows in various combustors. In view of different treatments for solid phase, two kinds of numerical methods commonly exist in the literature, i.e., Eulerian-Eulerian and Eulerian-Lagrangian methods. The former treats the gas and solid phases as interpenetrating continua, and the kinetic theory of granular flows (KTGF) is applied to model inter-particle collisions (Gidaspow, 1994). Although this method has the advantage of superior computational convenience, it cannot identify discrete particles, which suppresses its application in exploring the fundamentals of heat and mass transfer (Wang, 2020). In contrast, as one of Eulerian-Lagrangian methods, CFD-DEM approach resolves the inter-particle collisions and describes the inter-phase interactions by local-filtered drag correlations, delivering a high-fidelity way to explore hydrodynamics and thermochemical characteristics of gas-sold flows in fluidised beds. Zhu et al. (2008) reviewed the extensive CFD-DEM applications in granular processes, e.g., hoppers, mixers, drums, and pneumatic conveying. Hou et al. (2012) and Zhao et al. (2009) extended this approach to study heat transfer in fluidised beds operated under different fluidisation regimes and within an immersed tube. However, these studies are mainly carried out based on heat transfer simulations without chemical reactions considered. It is noted that heat fluxes released from heterogeneous and homogeneous reactions will directly affect the bed hydrodynamics and heat transfer characteristics during fluidised bed combustion (Liu et al., 2011). Nowadays, the CFD-DEM approach is extended to couple with thermochemical sub-models to study food drying (Azmir et al., 2019; Mohseni and Peters, 2016), biomass gasification (Ku et al., 2015; Ostermeier et al., 2019), and coal combustion (Geng and Che, 2011; Shimura and Matsuo, 2019). Excellent work has also been done to apply the CFD-DEM approach in modelling ironmaking blast furnaces, such as the softening behaviour of iron ore pellets (Baniasadi et al., 2018; Yang et al., 2015), the direct reduction of iron ore (Kinaci et al., 2020; Peters and Hoffmann, 2016), and so on. Nevertheless, the conductive heat transfer mode is neglected or only partially considered in these studies. The particle-scale analysis for each heat transfer mode's contribution during the combustion is unavailable, so as the mass transfer properties. Moreover, inert particles (e.g., sand) and reactive particles (e.g., coal, biomass) significantly differ in density and size. The continuous mass loss of fuel particles because of chemical reactions also causes great disparities in size. The polydispersity of particles is demonstrated to remarkably influence the bed hydrodynamics by underestimating the drag force for large particles and overestimating it for small particles (Beetstra et al., 2007). The CFD-DEM simulation of dense gas-solid reacting systems considering the polydispersity effect was not reported in the literature.

Accordingly, the heat and mass transfer behaviours and their relationship with bed hydrodynamics (e.g., bubble evolution, solid mixing, and solid dispersion) are numerically studied. The novelty of the present work lies in the following aspects: (i) development of a reactive CFD-DEM model featuring particle size polydispersity and thermochemical sub-models; (ii) the first quantitative analysis of the contribution of each heat transfer mode in combustion in a fluidised bed in view of reactive solid fuel (i.e., char) and inert bed material (i.e., sand). The present article is structured as follows: Section 2 gives governing equations and sub-models for heat and mass transfer. Section 3 presents simulation conditions and numerical settings. Section 4.1 shows the model validation regarding binary particle mixing, particle temperature, and particle diameter in BFB reactors. The general flow patterns of the char combustion are shown in Section 4.1, followed by the analysis of mixing and dispersion of solid species on heat and mass transfer behaviours in Section 4.2. Section 4.3 explores each heat transfer mode's contribution. The mass, momentum, and energy exchanges at the particle scale are illuminated in Section 4.4. Conclusion is drawn in Section 5.

2. Mathematical model

In this work, heat and mass transfer sub-models are considered in the CFD-DEM framework to simulate the thermochemical characteristics of char combustion in a BFB reactor. Generally, the gas phase is described by Navier-Stokes equations, while the solid phase is governed by the DEM. The char combustion process is also considered. Flow dynamics and thermochemical sub-models are coupled via source terms.

2.1. Gas phase model

Regarded as a continuum, the gas phase is governed by conservation equations. Mass conservation equation is given by:

$$\frac{\partial(\varepsilon_g\rho_g)}{\partial t} + \nabla\cdot\left(\varepsilon_g\rho_g\mathbf{u}_g\right) = \sum_{n=1}^{N_g} R_{gn} \tag{1}$$

where $\mathbf{u}_g$ is the velocity. N_g is the total number of species. R_{gn} is the volumetric change rate of nth species due to heterogeneous reactions.

Momentum conservation equation is given by:

$$\frac{\partial\left(\varepsilon_g\rho_g\mathbf{u}_g\right)}{\partial t} + \nabla\cdot\left(\varepsilon_g\rho_g\mathbf{u}_g\mathbf{u}_g\right) = \nabla\cdot\bar{\bar{S}}_g + \rho_g\varepsilon_g\mathbf{g} - \sum_{m=1}^{M}\mathbf{I}_{gm} \tag{2}$$

where $\bar{\bar{S}}_g$ is the gas stress tensor, evaluated by a modified k-ε turbulence model (Wang et al., 2019). The turbulence-particle interaction is neglected in this work due to the large particle size (d_p) and the large particle to gas density ratio ($\rho_p/\rho_f \sim 10^3$) used in the following simulation cases. This strategy can be found in many CFD-DEM simulations (Tang et al., 2017; Wang et al., 2019; Zhu et al., 2007).

Interphase momentum exchange term ($\mathbf{I}_{gm}$) is given by:

$$\begin{aligned}\mathbf{I}_{gm} &= \frac{1}{V_c}\sum_{i=1}^{N_p}\mathbf{F}_d \\ &= \frac{1}{V_c}\sum_{i=1}^{N_p}\left(-\nabla P_g(x_i)V_i + \frac{\beta V_i}{(1-\varepsilon_g)}\left(\mathbf{u}_g(x_i) - \mathbf{v}_p\right)\right)\end{aligned} \tag{3}$$

where $\mathbf{F}_d$ is the fluid force (including the pressure gradient force and drag force) acting on particle i. V_c and V_i are the cell volume and particle volume, respectively. $\mathbf{v}_p$ is the particle velocity. β is the gas-solid momentum exchange coefficient, commonly calculated by various drag correlations (Ergun and Orning, 1949; Gidaspow, 1994; Hill et al., 2001; Wen, 1966). During char combustion in the BFB combustor, the particle mass will be continuously reduced

due to chemical reactions, which causes great particle size disparities. The drag model based on the monodisperse system should be modified with the polydispersity effect considered (Beetstra et al., 2007):

$$\beta = \frac{18\mu_g \varepsilon_g (1-\varepsilon_g)}{d_{p,i}^2} F_i \tag{4}$$

$$F_i = \left(\varepsilon_g y_i + (1-\varepsilon_g) y_i^2 + 0.064 \varepsilon_g y_i^3\right) F \tag{5}$$

$$F = \frac{10(1-\varepsilon_g)}{\varepsilon_g^2} + \varepsilon_g^2 \left(1 + 1.5(1-\varepsilon_g)^{0.5}\right) + \frac{0.413 Re_p}{24\varepsilon_g^2}\left[\frac{\varepsilon_g^{-1} + 3\varepsilon_g(1-\varepsilon_f) + 8.4 Re_p^{-0.343}}{1 + 10^{3(1-\varepsilon_g)} Re_p^{-0.5-2(1-\varepsilon_g)}}\right] \tag{6}$$

$$y_i = \frac{d_{p,i}}{d_p} \tag{7}$$

$$d_p = \frac{\sum_{i=1}^{c} N_i d_{p,i}^3}{\sum_{i=1}^{c} N_i d_{p,i}^2} \tag{8}$$

$$\mathrm{Re}_p = \frac{\rho_g \varepsilon_g |\mathbf{u}_g - \mathbf{v}_p| \mathrm{d}_p}{\mu_g} \tag{9}$$

where $d_{p,i}$ is the diameter of particle i; d_p is the Sauter mean diameter of particles; c is the species presented in the system; Re_p is the particle Reynolds number.

Energy conservation equation is written as:

$$\frac{\partial\left(\varepsilon_g \rho_g C_{p,g} T_g\right)}{\partial t} + \nabla\left(\varepsilon_g \rho_g \mathbf{u}_g C_{p,g} T_g\right) = \nabla \cdot \left(\varepsilon_g \kappa_g \nabla T_g\right) + Q_{gp} - \Delta H_{rg} + \gamma_{Rg}\left(T_{Rg}^4 - T_g^4\right) \tag{10}$$

where $C_{p,g}$ is specific heat capacity; κ_g is the thermal conductivity. Q_{gp} is the volumetric convective heat flux. ΔH_{rg} is the volumetric flux due to gas combustion.

Species conservation equation is written as:

$$\frac{\partial(\varepsilon_g \rho_g X_n)}{\partial t} + \nabla \cdot \left(\varepsilon_g \rho_g \mathbf{u}_g X_n\right) = \nabla \cdot \left(\varepsilon_g \rho_g D_n \nabla X_n\right) + R_{gn} \tag{11}$$

where X_n and D_n represent mass fraction and diffusivity coefficient of nth gas species, respectively.

The relationship between gas density and gas temperature is solved by the equation of state:

$$\rho_g = \frac{P_g MW_g}{R_g T_g} \tag{12}$$

where MW_g denotes molecular weight; R_g stands for universal gas constant.

2.2. Solid phase model

Dynamics of every particle is described by Newton's law of motion while inter-particle collisions are denoted by a soft-sphere contact model (Cundall and Strack, 1979). In the present work, only the gravity, pressure gradient force, and collision force exerting on a specific particle are considered. Other forces (e.g., lift force, Basset force, virtual mass force) are neglected due to their insignificance in modelling gas-solid fluidised bed systems ($\rho_f/\rho_p \sim 10^{-3}$) as suggested in the review paper by Zhu et al. (2007). Thus, governing equations for a specific particle are written as (Garg et al., 2012):

$$m_p \frac{d\mathbf{v}_p}{dt} = m_p \mathbf{g} + \mathbf{F}_d + \mathbf{F}_c \tag{13}$$

$$I_p \frac{d\omega_p}{dt} = \sum_{j=1, j\neq i}^{k} \left(L\mathbf{n} \times \mathbf{F}_{ij}^t\right) \tag{14}$$

where the fluid force $\mathbf{F}_d$ has been given in Eq. (3). L is the distance between the contact point and particle centroid, which can be calculated according to the literature (Garg et al., 2012). $\mathbf{F}_c$ is the contact force because of inter-particle collisions, which includes the elastic contact force and viscous damping force and is given by:

$$\mathbf{F}_c = \sum_{j=1, j\neq i}^{k} \left(\mathbf{F}_{ij}^n + \mathbf{F}_{ij}^t\right) \tag{15}$$

$$\mathbf{F}_{ij}^n = -\left(k_{n,ij}\delta_{n,ij} - \eta_{n,ij}\dot{\delta}_{n,ij}\right)\mathbf{n}_{ij} \tag{16}$$

$$\mathbf{F}_{ij}^t = \begin{cases} -\left(k_{t,ij}\delta_{t,ij} - \eta_{t,ij}\dot{\delta}_{t,ij}\right)\mathbf{t}_{ij} \text{ for } \left|\mathbf{F}_{ij}^t\right| \leqslant \mu\left|\mathbf{F}_{ij}^n\right| \\ -\mu\left|\mathbf{F}_{ij}^n\right|\mathbf{t}_{ij} \text{ for } \left|\mathbf{F}_{ij}^t\right| > \mu\left|\mathbf{F}_{ij}^n\right| \end{cases} \tag{17}$$

The calculation of variables relating to the particle properties (e.g., spring stiffness k, damping coefficient η, friction coefficient μ) can refer to the literature (Garg et al., 2012). Linear spring-dashpot (LSD) model is used instead of a non-linear Hertzian model because the former model has been demonstrated to provide higher efficiency with the high numerical accuracy guaranteed (Wang et al., 2020).

During char combustion in the BFB, heat transfer exerting on a specific particle includes four modes: convection, conduction, radiation, and reaction. In the simulation, the particle is assumed as isothermal, which means the temperature gradients inside the particle are neglected. The energy balance of particle i is given by:

$$m_p C_{p,i} \frac{dT_{p,i}}{dt} = Q_{gp,i} + Q_{pp,i} + Q_{pgp,i} + Q_{rad,i} - \Delta H_{rs} \tag{18}$$

where $Q_{pp,i}$ and $Q_{pgp,i}$ represent the conductive heat flux via particle-particle and particle-gas-particle paths. $Q_{gp,i}$, $Q_{rad,i}$, and ΔH_{rs} are the heat flux stemming from convection, radiation, and chemical reactions.

2.3. Heat transfer model

This section outlines four typical heat transfer modes. The convective heat transfer flux is calculated as:

$$Q_{gp,i} = h_{pg,i} A_{p,i} (T_g - T_{p,i}) \tag{19}$$

$$h_{pg,i} = \frac{\mathrm{Nu}_{p,i}\kappa_g}{d_{p,i}} \tag{20}$$

$$\mathrm{Nu}_{p,i} = 2.0 + 0.6 Re_{p,i}^{1/2} \mathrm{Pr}^{1/3} \tag{21}$$

where $\mathrm{Nu}_{p,i}$ is the particle Nusselt number; $A_{p,i}$ ($= \pi d_{p,i}^2$) is the particle surface area; Pr (=$\mu_g C_{p,g}/\kappa_g$) is the Prandtl number.

The conductive heat transfer includes two paths, i.e. direct heat transfer via a particle-particle path ($Q_{pp,ij}$) and non-direct heat transfer via a particle-gas-particle path ($Q_{pfp,ij}$). The former one is given by (Batchelor and O'Brien, 1977):

$$Q_{pp,ij} = 4\frac{\kappa_{p,i}\kappa_{p,j}}{\kappa_{p,i} + \kappa_{p,j}} R_{c,ij} (T_{p,j} - T_{p,i}) \tag{22}$$

$$R_{c,ij} = \sqrt{R_{p,j}^2 - \left(\frac{R_{p,j}^2 - R_{p,i}^2 + l_{ij}^2}{2l_{ij}}\right)^2} \tag{23}$$

where $R_{c,ij}$ is the radius of the contact surface.

The particle-gas-particle conductive heat flux $Q_{pgp,ij}$ is through a gas layer wrapped around particle i with a thickness of $0.2d_p$. Integrating from the lower bound R_{in} to the outer bound R_{out} of the contact region, $Q_{pgp,ij}$ is given by (Musser, 2011):

$$R_{c,ij} = \sqrt{R_{p,j}^2 - \left(\frac{R_{p,j}^2 - R_{p,i}^2 + l_{ij}^2}{2l_{ij}}\right)^2} \tag{24}$$

$$Q_{pgp,ij} = \kappa_g\left(T_{p,j} - T_{p,i}\right)\int_{R_{in}}^{R_{out}} \frac{2\pi r}{l_{ij} - \left(\sqrt{R_{p,i}^2 - r^2} + \sqrt{R_{p,j}^2 - r^2}\right)} dr \tag{25}$$

$$R_{in} = R_{c,ij} = \begin{cases} 0 \; l_{ij} > \left(R_{p,i} + R_{p,j}\right) \\ \sqrt{R_{p,j}^2 - \left(\frac{R_{p,j}^2 - R_{p,i}^2 + l_{ij}^2}{2l_{ij}}\right)^2} \; l_{ij} \leqslant \left(R_{p,i} + R_{p,j}\right) \end{cases} \tag{26}$$

$$R_{out} = R_{f,ij} = \sqrt{\left(R_{p,j} + d\right)^2 - \left(\frac{\left(R_{p,j} + d\right)^2 - R_{p,i} + l_{ij}^2}{2l_{ij}}\right)^2} \tag{27}$$

Due to the high temperature (>600 °C) in the BFB reactor, the radiative heat transfer should be considered. This heat transfer mode is calculated by considering the environmental temperature T_{env} and the particle properties (e.g., emissivity $e_{p,i}$). Assuming a spherical sub-domain with a default diameter of $1.5d_p$, T_{env} can be defined as the combination of mean particle temperature and gas temperature in this sub-domain (Zhou et al., 2009). Thus, the radiative heat flux $Q_{rad,i}$ is given by:

$$Q_{rad,i} = e_{p,i}A_{p,i}\sigma\left(T_{env}^4 - T_{p,i}^4\right) \tag{28}$$

$$T_{env} = \varepsilon_g T_{g,\Omega} + \left(1 - \varepsilon_g\right)\frac{1}{N_{p,\Omega}}\sum_{j=1\, j\neq i}^{N_{p,\Omega}} T_j \tag{29}$$

where $T_{g,\Omega}$ and $N_{p,\Omega}$ denote the gas temperature and particle number in the sub-domain, respectively.

The heat of reaction associated with the gas phase (ΔH_{rg}) is computed as the difference in enthalpies of the gaseous products and reactants. The heat of reaction (ΔH_{rs}) associated with the solid phase is computed as the difference in enthalpies of the solid products and reactants.

2.4. Chemical reaction model

During the char combustion, heterogeneous reactions and homogeneous reactions simultaneously take place. Generally, the mass loss is given by:

$$\frac{dm_p}{dt} = \sum_{n=1}^{N_s} R_{sn} \tag{30}$$

The particle mass is given as the sum of each species as:

$$m_p = \sum_{n=1}^{N_s} X_{pn} m_p \tag{31}$$

The variation of nth species because of reactions is given by:

$$\frac{d\left(X_{pn}m_p\right)}{dt} = R_{sn} \tag{32}$$

Thus, the mass fraction of nth species (X_{pn}) is given by:

$$\frac{dX_{pn}}{dt} = \frac{1}{m_p}\left(R_{sn} - X_{pn}\sum_{n=1}^{N_s} R_{sn}\right) \tag{33}$$

In this work, the oxidation of the char particle is considered as the heterogeneous reaction (R1), written as:

$$C_{(s)} + 0.5\ O_2 \rightarrow CO \tag{R1}$$

For this char-oxygen reaction (R1), many models were reported in the literature. British and Field (1967) proposed a chemical reaction rate and gas film diffusion constant for the char-oxygen reaction. DeSai et al. (1978) explored the char-oxygen reaction without ash diffusion considered. Wen et al. (1982) and Syamlal and Bissett (1992) assumed that the reaction rate was much faster than either the film or ash diffusion and thus neglected it. In this work, the shrinking core model is used, which accounts for external film diffusion and the reaction at the unreacted core's surface (Wen et al., 1982; Yoon et al., 1978). The reaction rate is formulated as:

$$r_1 = \left(\frac{1}{v_1 MW_{O_2}}\right)\frac{A_p\eta_p P_{O_2}}{\left(1/k_f + 1/k_r\right)} \tag{34}$$

where v_1, MW_{O_2}, and P_{O_2} are stoichiometric coefficient for the R1, the molecular weight of oxygen, and the partial pressure of oxygen, respectively. η_p is the particle number density, given as (Hobbs et al., 1993):

$$\eta_p = \frac{6\left(1 - \varepsilon_g\right)}{\pi d_p^3} \tag{35}$$

The film resistance k_f and the surface reaction resistance k_r are given as (DeSai et al., 1978; Wen et al., 1982):

$$k_f = \frac{D_{O_2}\mathrm{Sh}_{p,i}}{d_p\left(R_g/MW_{O_2}\right)T_g} \quad k_r = 8710r_d^2\exp\left(-\frac{13590}{T_p}\right)$$

where D_{O_2} is the diffusion coefficient for O_2, given as (Syamlal and Bissett, 1992; Wen et al., 1982):

$$D_{O_2} = 4.26 \times \left(\frac{T_g}{1800}\right)^{1.75} \tag{37}$$

The Sherwood number $\mathrm{Sh}_{p,i}$ can be calculated with the sand inhibitory effect considered (La Nauze et al., 1984):

$$\mathrm{Sh}_{p,i} = 2.0\varepsilon_g + 0.69\left(Re_{p,i}/\varepsilon_g\right)^{1/2}\mathrm{Sc}^{1/3} \tag{38}$$

$$\mathrm{Sc} = \frac{\mu_g}{\rho_g D_{O_2}} \tag{39}$$

where Sc denotes the Schmidt number.

With the progress of chemical reactions, particle size is reduced due to mass loss. The particle shrinkage may significantly influence the flow behaviours (e.g., particle trajectory, size-induced segregation) and the resulting thermochemical characteristics. In the shrinking core model, the particle density is assumed as a constant while the particle diameter changes throughout the reaction process as:

$$d_{p,i} = \left(\frac{6m_{p,i}}{\pi\rho_p}\right)^{1/3} \tag{40}$$

The oxidation of carbon dioxide is considered as the homogeneous reaction (R2), formulated as:

$$CO + 0.5\ O_2 \rightarrow CO_2 \tag{R2}$$

The reaction rate for R2 is given as (Dryer and Glassman, 1973):

$$r_2 = 3.98 \times 10^{14}\exp\left(-\frac{1.67 \times 10^5}{R_g T_g}\right)[CO][H_2O]^{0.5}[O_2]^{0.25} \tag{41}$$

2.5. Numerical scheme

The governing equations are discretised based on the finite volume method (FVM). The discretisation of governing equations in space and time is given as follows. The equations for kinetic motion, heat transfer, and species transport of solid phase are integrated using a first-order Euler scheme. Since high-order discretisation schemes commonly lead to difficult convergence, the governing equations for gas pressure, volume fraction, momentum, energy, mass fraction, granular energy, scalar/k-ε are discretised by a first-order upwind scheme. A SIMPLE algorithm solves the coupling between the gas velocity and gas pressure. A soft-sphere contact model handles inter-particle collisions, while volumetric drag correlations describe inter-phase interactions.

Chemical reaction sub-models involve the oxidation of char and carbon oxide (CO), termed as the heterogeneous reaction and homogeneous reaction, respectively. Gas-solid flows are coupled with chemical reactions via the exchange of mass, momentum, and energy in a conservation manner. For the CFD part, Courant-Friedrich-Lewy (CFL) number is used to monitor the calculation procedure as (Ferziger and Peric, 2012):

$$\mathrm{CFL} = \Delta t_{\mathrm{CFD}} \max\left(\frac{|\mathbf{u}_f|}{\Delta x}\right) < 1 \tag{42}$$

where Δt_{CFD} and Δx stand for the gas time-step and the grid size, respectively. The solid time-step has to be smaller than a specific value to guarantee numerical stability of multiple collisions (Tsuji et al., 1993). In this work, the solid time-step is specified as 1/50 of the minimum collision time during the simulation. All the mathematical models and numerical schemes are implemented on an opensource software package MFIX via a user-defined function (UDF). Simulation cases are performed on the platform of National Computational Infrastructure (NCI), a High-performance Computing (HPC) system with large amounts of cores (CPU/GPU) in Australia. In the NCI's supercomputer Gadi, each node is outfitted with Intel Xeon Platinum 8274 (Cascade Lake) CPUs @ 3.2 GHz.

3. Simulation conditions and computational settings

The investigated object is a lab-scale BFB reactor with the width, height, depth of 90 mm, 630 mm, 12 mm, respectively (Fig. 1). The bed depth is $4d_p$ (d_p = 3 mm). The grid number is 10, 70, and 2 in X, Y, and Z directions. Cell size ranges from 6 mm to 9 mm, 2 ~ 3 times the particle diameter, which meets the convectional CFD-DEM requirement (Clarke et al., 2018). The thermophysical properties (e.g., diameter, density, thermal conductivity, specific heat, emissivity, collision constants) of sand and char are summarised in Table 1. The equation of state determines the gas density, while other gas thermophysical properties (e.g., viscosity, thermal conductivity, specific heat) are calculated based on the thermal database (Bird, 2002; Burcat and Ruscic, 2005).

Initially, sand particles as bed material are generated in an ordered manner in the bed, while char particles are generated above the bed material. The char and sand have 300 K and 1073 K in initial temperature, respectively. Gas flow with a superficial gas velocity of 3.0 m/s is introduced to fluidise particles.

The gas inlet is set as uniform velocity and temperature boundary conditions; the outlet is specified at an atmospheric pressure boundary condition; the wall is no-slip. The gas time-step is set as 1×10^{-5} s, which can be dynamically adjusted during the simulation based on the CFL criterion. Running on the NCI's

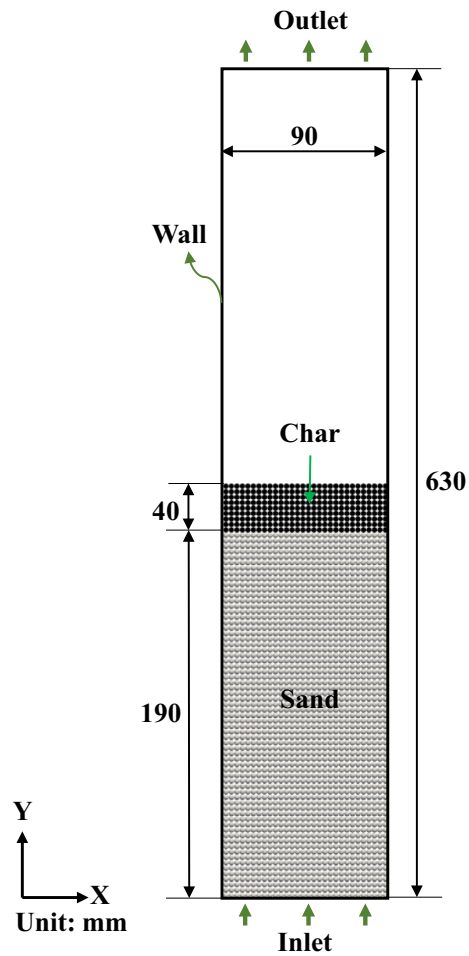

Fig. 1. Geometry and dimensions of the investigated bubbling fluidised bed reactor.

Table 1
Operating conditions and thermophysical properties.

Parameters	value	Unit
Bed dimension (x, y, z)	90, 630, 12	mm
Cell Number (N_x, N_y, N_z)	10, 70, 2	–
Bed temperature (T_b)	1073	K
Particle phase		
Material	Sand/Char	–
Number (N_p)	7940/1080	–
Diameter (d_p)	3.0/3.0	mm
Density (ρ_p)	2650/2100	$kg \cdot m^{-3}$
Temperature (T_p)	1073/300	K
Thermal conductivity (κ_p)	0.84/150	$W \cdot m^{-1} \cdot K^{-1}$
Specific heat ($C_{p,p}$)	800/836 + 1.53T_p	$J \cdot kg^{-1} \cdot K^{-1}$
Emissivity (e_p)	0.7/0.7	–
Spring stiffness (k_n)	1000/1000	$N \cdot m^{-1}$
Restitution coefficient (e)	0.9/0.9	–
Friction coefficient (μ_p)	0.1/0.1	–
Gas phase		
Density (ρ_g)	Equation of state	–
Viscosity (μ_g)	Thermo. Database[a]	$kg \cdot m^{-1} \cdot s^{-1}$
Thermal conductivity (κ_g)	Thermo. Database[a]	$W \cdot m^{-1} \cdot K^{-1}$
Specific heat capacity ($C_{p,g}$)	Thermo. Database[b]	$J \cdot kg^{-1} \cdot K^{-1}$
Superficial gas velocity (U_0)	3.0	$m \cdot s^{-1}$

Note: marks a and b mean the data are calculated based on the thermal database referring to Bird (2002) and Burcat and Ruscic (2005), respectively.

supercomputer Gadi with 8 CPU cores, each case takes about 25 h for a physical time of 200 s.

4. Results and discussion

4.1. Model validation

The CFD-DEM approach has been well validated towards the cold particulate system (Wang et al., 2017; Yue et al., 2019) and has been extended to study thermochemical systems (Cui et al., 2020; Wang and Shen, 2020) within monodisperse particles. This work extends the CFD-DEM framework with the polydispersity effect as well as thermochemical sub-models integrated. Thus, the developed model is validated regarding two aspects, i.e., the mixing of binary particles in a BFB and char combustion in a BFB combustor.

The model is first applied to an experiment of binary particles by Jiang et al. (2018). The test rig is a lab-scale BFB with 0.1 m × 0.34 m × 0.014 m. Different types of particles are initially packed with a mass of 20.2 g and 13.5 g. Large particles are 2.5 mm and 1450 kg/m^3 in diameter and density, respectively. Small particles are 1.8 mm and 985 kg/m^3 in diameter and density, respectively. Gas flow with a superficial gas velocity of 2.8 m/s is introduced to fluidise packed particles. The particle mixing process is identified by the mixing index, which is given by (Lacey, 1954):

$$\mathrm{MI} = \frac{\sigma_0^2 - S^2}{\sigma_0^2 - \sigma_r^2} \tag{43}$$

$$\sigma_0^2 = \bar{c}\left(1-\bar{c}\right);$$
$$\sigma_r^2 = \bar{c}\left(1-\bar{c}\right)/\bar{n};$$
$$S = \sqrt{\frac{1}{N-1}\sum_{i=1}^{N}\left(\bar{c}-c_i\right)^2} \tag{44}$$

where σ_0^2 and σ_r^2 are the variance of fully segregated and mixed solid mixing, respectively. N denotes the total number of sampling cells. $\bar{c}$ is the average concentration of one component. c_i is the solid concentration of one component in a sampling cell. $\bar{n}$ denotes the average particle number in a sampling cell, which is used for mono-disperse systems. In the poly-disperse system, the concept of the equivalent number $\bar{n}_e$ is used (Jiang et al., 2018). The variance S is formulated as:

$$S = \sqrt{\frac{1}{k_t}\sum_{i=1}^{N} k_i\left(\bar{c}-c_i\right)^2} \tag{45}$$

$$k_t = \sum_{i=1}^{N} k_i \tag{46}$$

where k_i is the weighting factor in sample i and k_t is the total weighting factor. Detailed calculation procedure can refer to the literature (Jiang et al., 2018). MI commonly ranges from zero to unity. MI = 0 means a fully segregated state while MI = 1 represents a perfectly mixed state.

As shown in Fig. 2, the mixing index rapidly rises at the initial time and fluctuates around a fixed value after reaching an equilibrium state. The profile calculated by the polydisperse drag model shows good agreement with experimental data while that by monodisperse drag model underestimates it. It is because the monodisperse one underestimates the solid motion of large particles and overestimates that of small particles. Hence, the polydisperse drag model should be used to simulate BFB systems within disparities in particle size to reproduce bed hydrodynamics accurately.

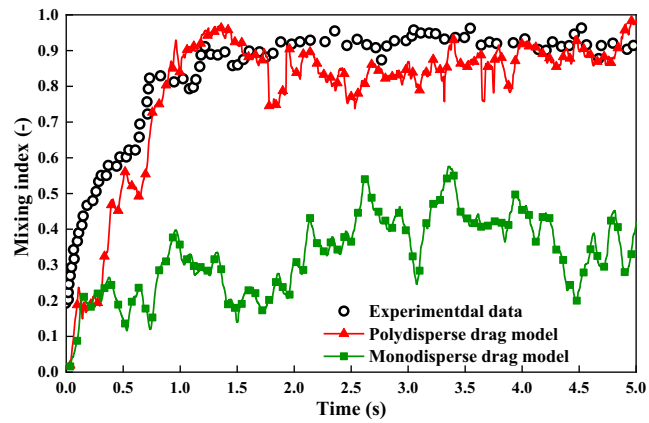

Fig. 2. Comparison of time-evolution mixing index between current simulation and experimental data (Jiang et al., 2018).

The model is subsequently validated about heat and mass transfer of char combustion against the measurements in a lab-scale BFB combustor (Hayhurst and Parmar, 2002). The bed has a rectangular region with 40 mm × 160 mm × 3 mm. Sand particles with a total number of 36,000 are initially packed. A char particle is suspended at the bed surface. Sand and char particles have a diameter of 0.5 mm and 3.0 mm, respectively. They have a density of 2650 kg/m^3 and 2100 kg/m^3, respectively. The initial bed temperature and char temperature are 1173 K and 300 K, respectively. Airflow with a superficial gas velocity of 0.308 m/s is introduced at 1173 K. Other gas-solid thermophysical parameters can refer to the literature (Geng and Che, 2011). Residence time means the time the char particle resides inside the reactor from the beginning to the present, which is given by:

$$t_{res} = t - t_0 \tag{47}$$

where t_{res} represents the residence time, t means the present time instant, and t_0 stands for the beginning time, which is zero in the validation case.

Fig. 3 gives the evolution of char temperature and char diameter with residence time in the bed. Generally, the char temperature rapidly increases from 300 K to about 1300 K. As time progresses, char temperature gradually rises. The fluctuations of the temperature profile result from intense inter-particle collisions, inter-phase interactions, and bubble-emulsion phase interactions. These interactions perform a significant influence on the gas-solid heat and mass transfer behaviours. The resulting fluctuations of gas temperature and gaseous product yields cause char temperature fluctuations. It is noted that the predicted char temperature agrees well with the experimental data. As shown in Fig. 2(b), the present model well predicts the variation of the char diameter.

Based on the above-mentioned validation, the established model is reasonable to simulate the physical and thermochemical properties of the char combustion process in the BFB combustor.

4.2. Typical flow patterns

Fig. 4 gives the time-evolution snapshots of instantaneous particle species, vertical velocity, temperature, and diameter. Char and sand particles are initially packed in two layers, respectively. Due to the density difference with sand material, char particles are initially floated at the bed surface, although several small bubbles are generated from the bottom (5 s–15 s). After the initial stage, the packed bed is expanded with the char particles entrained into

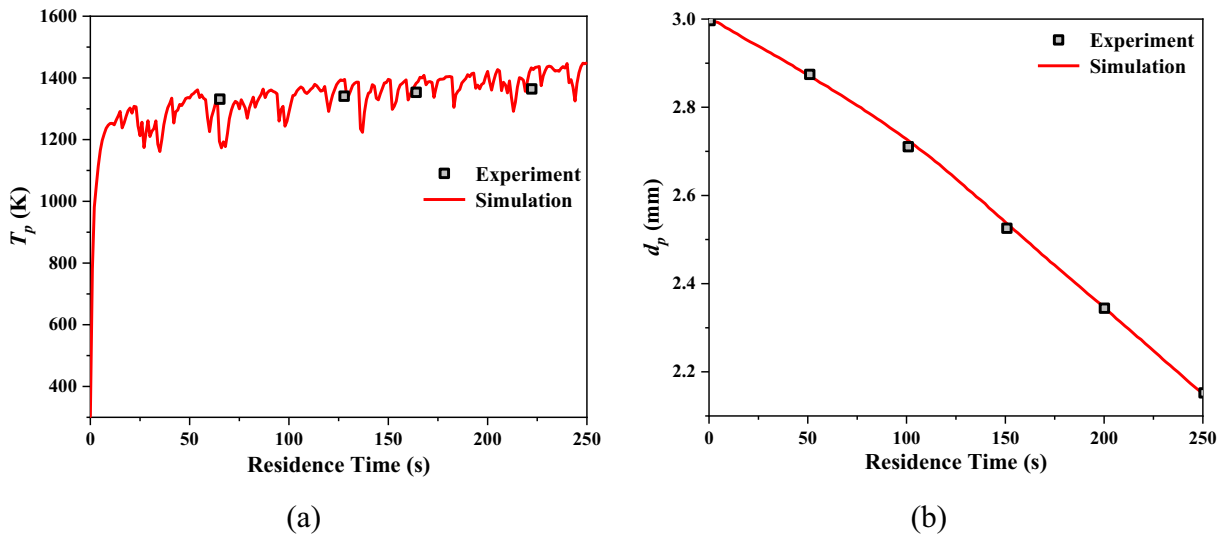

Fig. 3. Comparison of time-evolution char temperature (a) and char diameter (b) between current simulation and experimental data (Hayhurst and Parmar, 1998; Hayhurst and Parmar, 2002).

the emulsion phase because of drag force (20 s). As time marches, the volume of the gas phase will be increased due to heterogeneous (R2) and homogenous reactions (R2). Thus, larger bubbles are formed after the initial time (40 s). After rising and coalescence along with the bed height, these bubbles burst at the bed surface with particles scattered into the freeboard (50 s–200 s). As shown in Fig. 4b, particles rise in the core region and fall close to the wall. This solid back-mixing phenomenon causes internal particle circulation. Hence, the vigorous gas-solid interactions, mesoscale bubble dynamics, and internal circulation pattern intensify the mixing degree of char particles and sand particles in the bed.

The temperature of char particles rapidly increases to the bed temperature (1073 K) at the initial stage because of the absorption of heat flux from the gas phase (Fig. 4c). Char particles emerged in the hot air flow are simultaneously oxidised by oxygen (O_2), with a large amount of heat released. The released heat flux due to chemical reactions leads to the further increase of char temperature. As the reaction progresses, the excessed heat flux will increase the temperature of the bed material via the convection, conduction, and radiation patches. Thus, the bed temperature gradually increases and is larger than the inlet gas temperature (1073 K). A lower-temperature zone in the bottom corner of the bed can be observed because of convective heat transfer between low-temperature inlet gas and high-temperature bed material. The contribution from each heat transfer mode of char and sand particles will be discussed in the following section. Vigorous inter-phase heat and mass exchanges lead to the continuous consumption of char particles. The diameter of char particles will be decreased over time due to the heterogeneous reaction. After 200 s, the diameter of char particles approaches 2.4 mm.

The merit of the CFD-DEM approach is to capture the abundant physical information of each particle in the system. Exploring the particle trajectory is helpful for the understanding of the movement trend of different particle species. In this study, a tracer char particle located in the central bed surface and a tracer sand particle located in the central bed bottom are tracked. Fig. 5 shows the trajectory of the two particles. Because of non-linear multiphase flows, char and sand particles show chaotic motions. Tracer particles move horizontally and axially. The mean horizontal positions of char tracer and sand tracer are respectively 0.0426 m and 0.0452 m, while the mean axial positions of char tracer and sand tracer are respectively 0.176 m and 0.167 m. Thus, the motions of sand particles are nearly symmetrical along the central axis, while the motions of char particles are inclined to the left-side region of the bed. Due to density and size difference with sand particles, the char particles are highly influenced by the bubble dynamics. Identified by a threshold voidage of 0.75, the bubble evolution is shown in Fig. 6(a). The bubbles tend to generation, coalescence, and enlargement close to the left wall, which significantly influences the char particles than the sand particles. Moreover, the mean axial position of the char tracer is larger than that of the sand tracer because of density- and size-induced segregation phenomena, as reported in several experiments (Bai and Si, 2020; Cluet et al., 2015; Park and Choi, 2013). Different particle behaviours lead to the distinct thermochemical characteristics of char and sand particles.

Fig. 6(b-d) illustrates the contour plots of instantaneous gaseous species in the bed. O_2 introduced from the bottom reacts with floated char particles at the initial state (15 s) with CO released. The excessed oxygen will rapidly consume the CO with CO_2 produced. The O_2 shows an opposite distribution but a similar amount with the CO_2. The rheology of the solid phase at the micro-scale together with the wall restriction effect at the macro-scale leads to the asymmetry and non-uniform distribution of solid particles and gas species in the BFB reactor, which has been widely evidenced in the literature (Ku et al., 2015; Wang et al., 2020; Zhou et al., 2009).

4.3. Mixing and dispersion

The relative motion between the char particle and sand particle can be evaluated by the mixing index (MI), while the absolute motion of these two particle species can be assessed by the dispersion coefficient.

Inadequate solid mixing leads to non-uniform gas-solid distributions and further causes by-reactions and the resulting reduction of reactor performance (Beetham and Capecelatro, 2019; Liu and Chen, 2011; Yang et al., 2014). Fig. 7 illustrated the solid mixing under different gas inlet velocities. From the mesoscale view, the continuous evolution of bubbles provides the energy for the mixing of char and sand particles. Enlarging gas inlet velocity increases the bed height with larger-size bubbles generated. Generally, the mixing index (MI) rapidly rises to the maximum value and then fluctuates around the mean value after the system

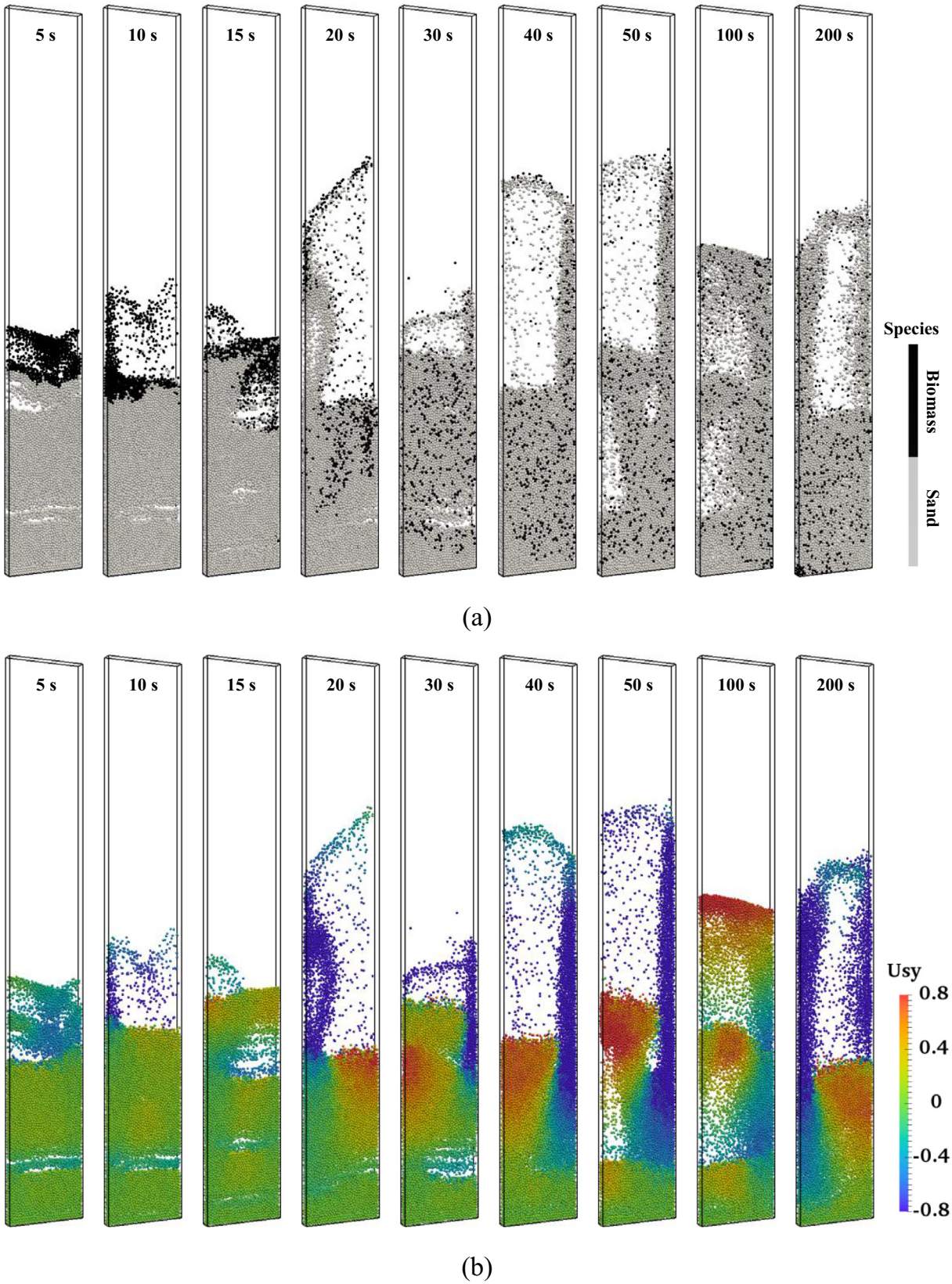

Fig. 4. Snapshots of instantaneous particle flow patterns during the char combustion process, U_0 = 3.0 m/s, T_b = 1073 K: (a) sand species; (b) particle vertical velocity (U_{sy}); (c) particle temperature (T_p); (d) particle diameter (d_p).

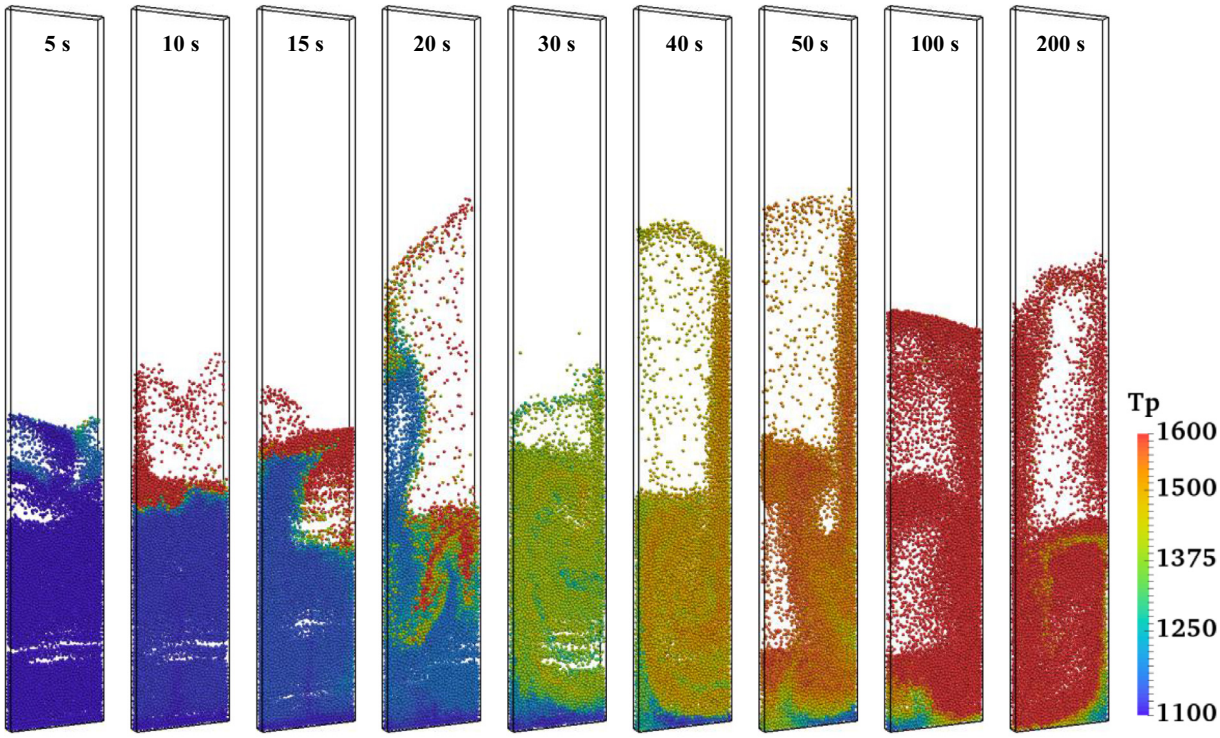

(c)

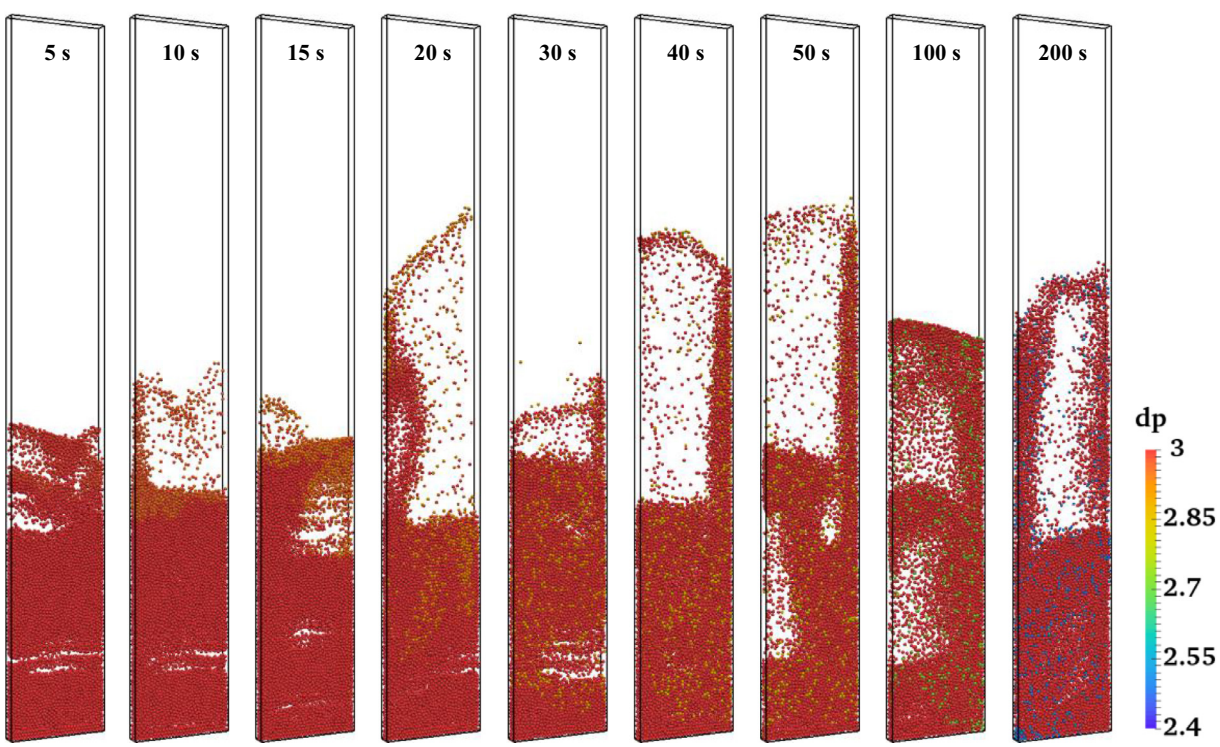

(d)

Fig. 4 (*continued*)

reaches an equilibrium state. The mean MI for three gas inlet velocities is respectively 0.828, 0.830, and 0.825. It is noted that the system cannot reach an ideal mixing state even though the gas inlet velocity is increased. Reasons lie in the density difference and the size difference between char particles and sand particles with the progress of the reactions. Interestingly, a dead zone mainly composed of sand particles is formed in the bottom corner due to the size-/density-induced segregation mechanism and bubble

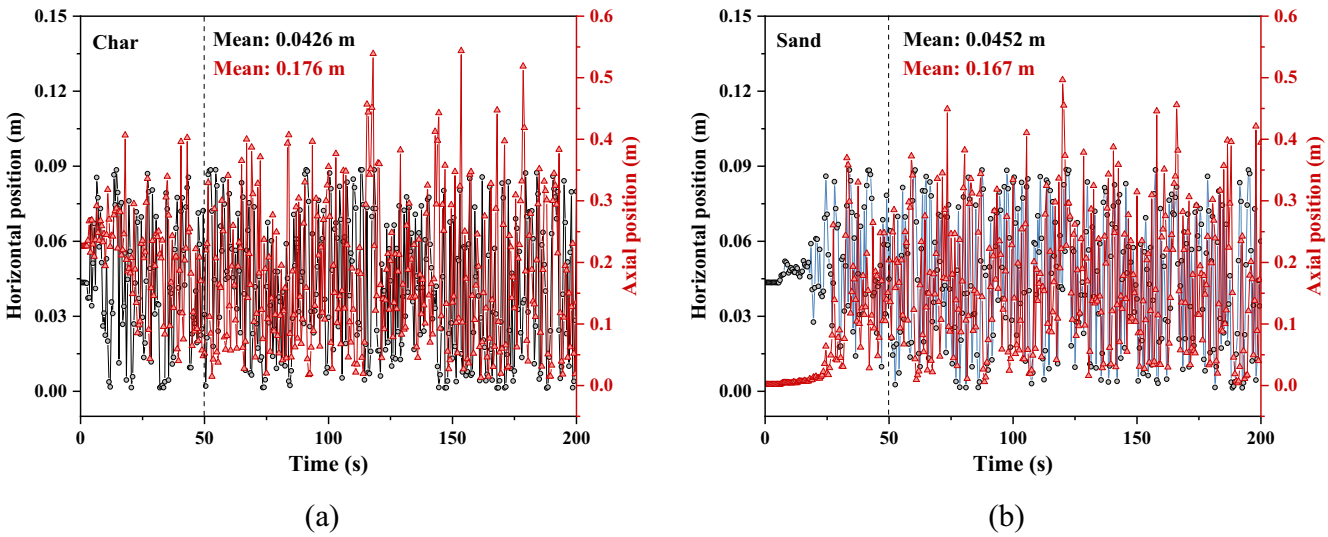

Fig. 5. Horizontal position (a) and axial position (b) of the char and sand particles in the bed, U_0 = 3.0 m/s, T_b = 1073 K.

entrainment effect. This phenomenon has been widely evidenced in the literature (Wang et al., 2015; Yang et al., 2019). Combining with Fig. 4a, the dead zone evolves both in time and space, i.e., its position may vary over time, e.g., at the left corner of the bed and then the right corner of the bed. The dead zone is formed after about 30 s, thus it is insensitive to the initial conditions. It will exist under different superficial gas velocities if it is still within the bubbling fluidisation regime. The dead zone without char particles may deteriorate heat and mass transfer of the whole system. Thus, it should be optimised when designing the BFB combustor.

The dispersion coefficient can characterise solid transportation in the fluidised bed. From the micro-scale view, solid dispersion highly influences solid mixing and solid residence time characteristics. According to the experimental and theoretical analysis in the literature (Breault, 2006; Liu and Chen, 2010; Sánchez-Prieto et al., 2017), the solid dispersion coefficient ranges from 0.0001 m^2/s to 0.1 m^2/s in fluidised beds. The particle's displacement can be calculated based on the inter-particle/phase interactions in a time interval. In the next time instant, the particle moves to a new position. Again, the displacement of this particle can be easily obtained. Hence, the trajectory of each particle is obtained. On the base of trajectory, the solid dispersion coefficient (D_i) for each particle is formulated at the micro-scale level (Liu and Chen, 2010):

$$D_i = \frac{(\Delta r_i)^2}{2\Delta t} \tag{48}$$

where Δr_i is particle displacement in the time interval Δt. To examine the transport mechanism of total particles, the average solid dispersion coefficient is calculated as:

$$D = \frac{1}{N_P}\sum_{i=1}^{N_P}\frac{(\Delta r_i)^2}{2\Delta t} = \frac{1}{N_P}\sum_{i=1}^{N_P}\frac{(r_i - r_{i0})^2}{2\Delta t} \qquad (i = 1, 2, ..., N_P) \tag{49}$$

where N_p is the particle number.

Fig. 8 gives the time-evolution solid dispersion coefficients. Due to the smaller density easier to be fluidised, the horizontal dispersion coefficient (Dx) for char particles more quickly reaches the maximum and fluctuates around the mean value of 1.049×10^{-3} m^2/s. In contrast, the longer relaxation time of sand particles due to the larger density makes them more slowly establish the equilibrium state around the mean value of 1.044×10^{-3} m^2/s. The char particle shows nearly the same frequency and magnitude of dispersion coefficients after the equilibrium state, indicating these two solid species are both dominated by the bubble-emulsion phase interactions. The axial dispersion coefficients (Dy) for char particle and sand particle are 0.1768 m^2/s and 0.1708 m^2/s, respectively. Hence, the axial dispersion coefficient is over one order of magnitude larger than the horizontal one, demonstrating the dominant role of the introduced gas flow in determining the bed hydrodynamics.

4.4. Heat transfer contribution

Four main heat transfer modes exist during the char combustion in the BFB combustor. Zhou et al. (2009) reported that the convection is larger than the radiation, followed by the conduction, under the condition of U_0 = 3.2 m/s and T_b = 1000 °C in a similar BFB. However, due to the neglection of chemical reactions in nearly all CFD-DEM studies regarding the heat transfer process (Lu et al., 2017; Wang et al., 2019; Zhang et al., 2020; Zhao et al., 2009), the contribution of the heat of reaction has not been elucidated so far.

Fig. 9 gives the contribution of four heat transfer modes of char and sand particles in the bed. The heat flux for each solid species is averaged by dividing their particle number to diminish the disparity of the particle amount. For the char particle, the heat fluxes from four modes fluctuate around fixed values. The fluctuations are mainly caused by inter-particle/phase interactions, bubble dynamics, and mesoscale flow structures (e.g., solid back-mixing, internal particle circulation). The particle-averaged heat fluxes from convection, conduction, radiation, and reaction are 0.00275 W, 0.00023 W, 0.01136 W, and 0.01375 W, respectively. The percentages of these four modes in the total flux are 9.79%, 0.82%, 40.44%, 48.95%, respectively. Thus, it is clearly noted that the radiation and heat of reaction dominate the heat transfer process of char particles during the BFB combustion. The convection performs a weak influence while the conduction is negligible. For the sand material, the heat fluxes from convection, conduction, and radiation oscillate around fixed values after 100 s. The particle-averaged heat fluxes from these three modes are 0.00245 W, 0.0000809 W, 0.00556 W, respectively. Thus, for the inert material during char combustion in the BFB reactor, the radiation performs the largest contribution of 68.72%, followed by the convection of 30.28%. The conduction of 1.0% can also be neglected during the simulation.

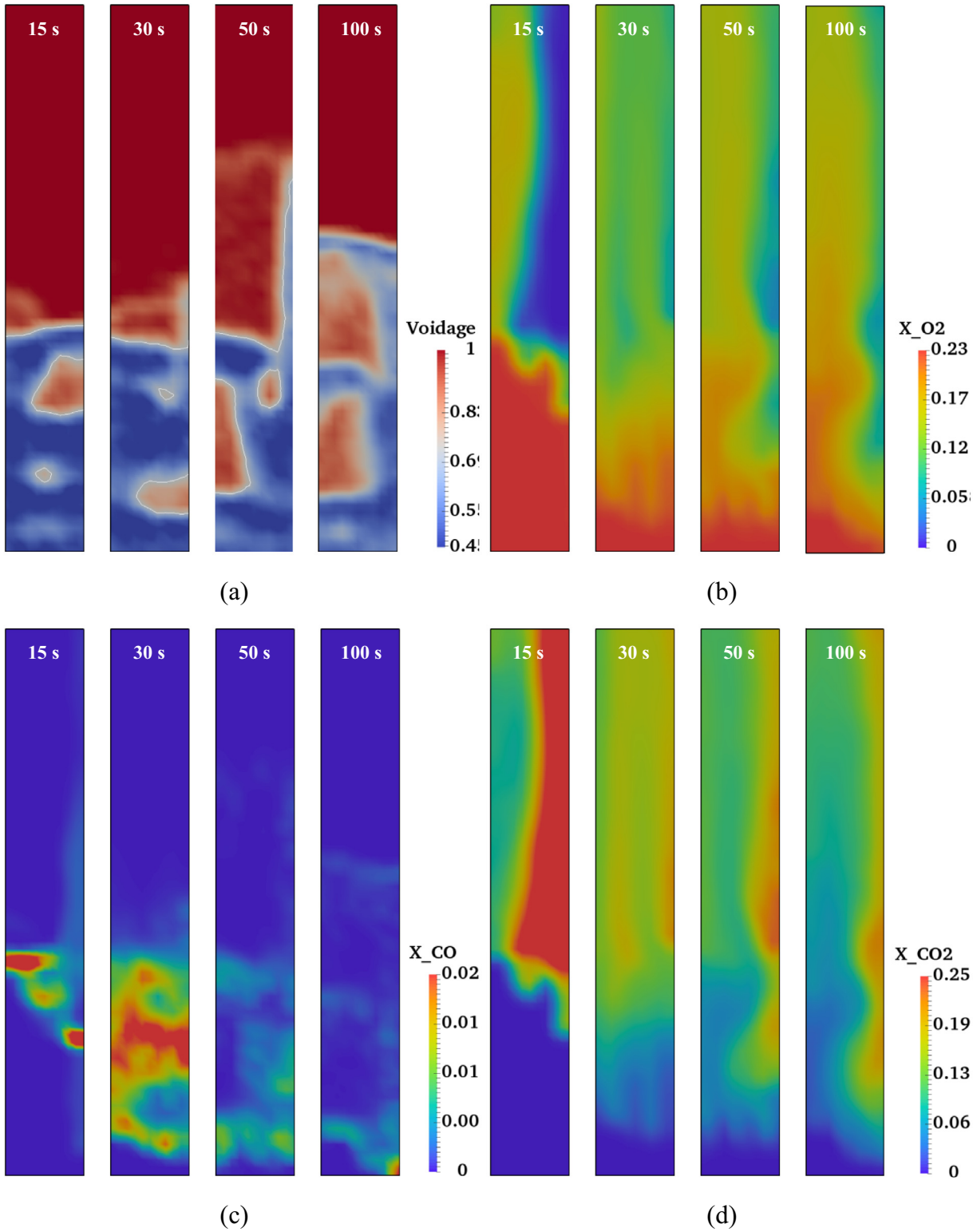

Fig. 6. Contour plots of gas properties in the central slice of the bed, U_0 = 3.0 m/s, T_b = 1073 K: (a) Voidage; (b) mass fraction of O_2; (c) mass fraction of CO; (d) mass fraction of CO_2.

4.5. Dimensionless number analysis

Hydrodynamics and heat/mass transfer behaviours of solid material during char combustion in the BFB reactor are closely related to the particle Reynolds number (Re_p), particle Nusselt number (Nu_p), and particle Sherwood number (Sh_p), respectively. Re_p is defined as the ratio of inertial forces to viscous forces within a fluid subjected to relative internal movement due to different fluid velocities. Nu_p is defined as the ratio of convection heat transfer to fluid conduction heat transfer under the same conditions. Sh_p represents the ratio of the convective mass transfer to the rate of diffusive mass transport. Fig. 10 gives the time-evolution profiles

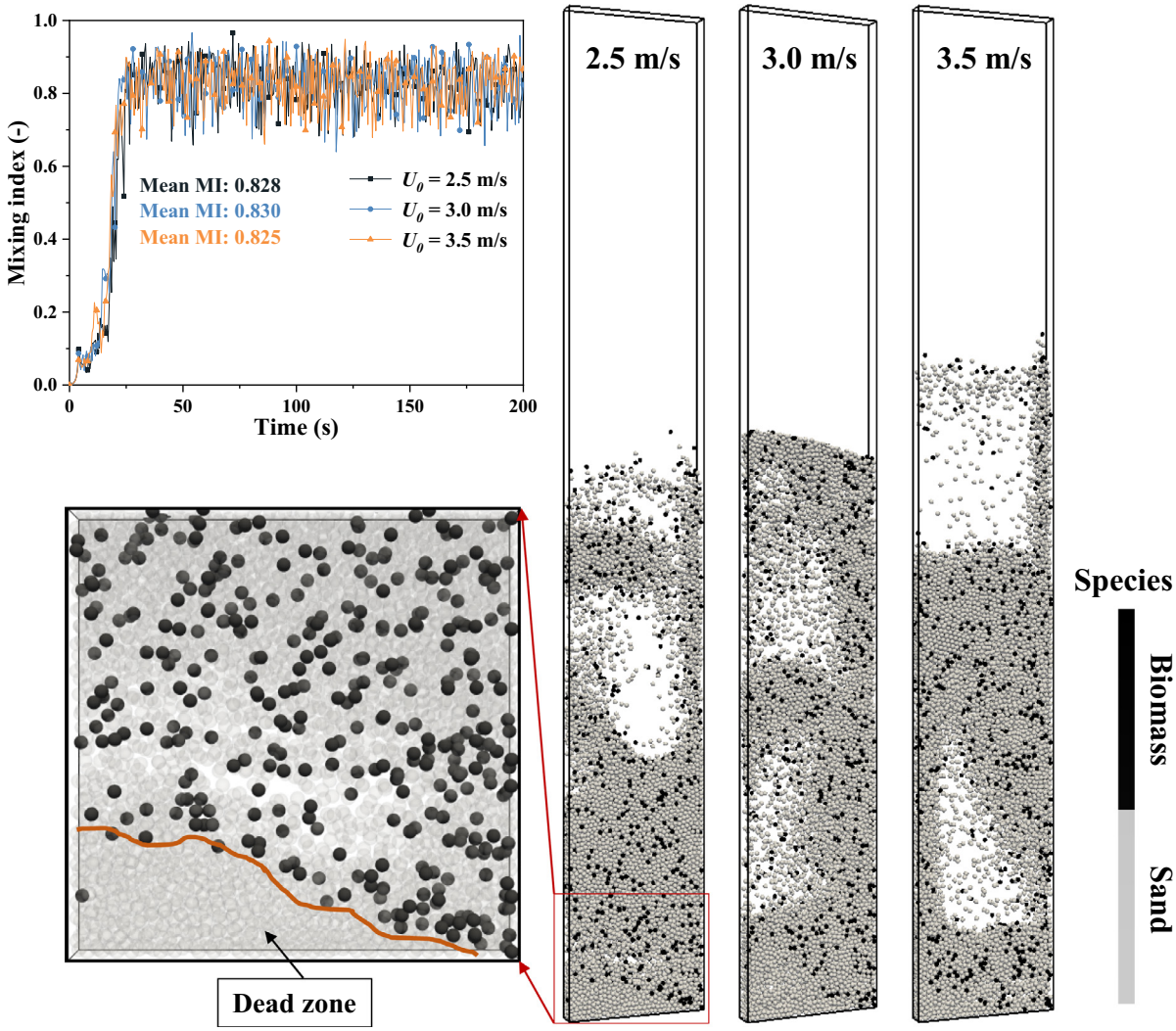

Fig. 7. Solid mixing in the bed under different gas inlet velocities.

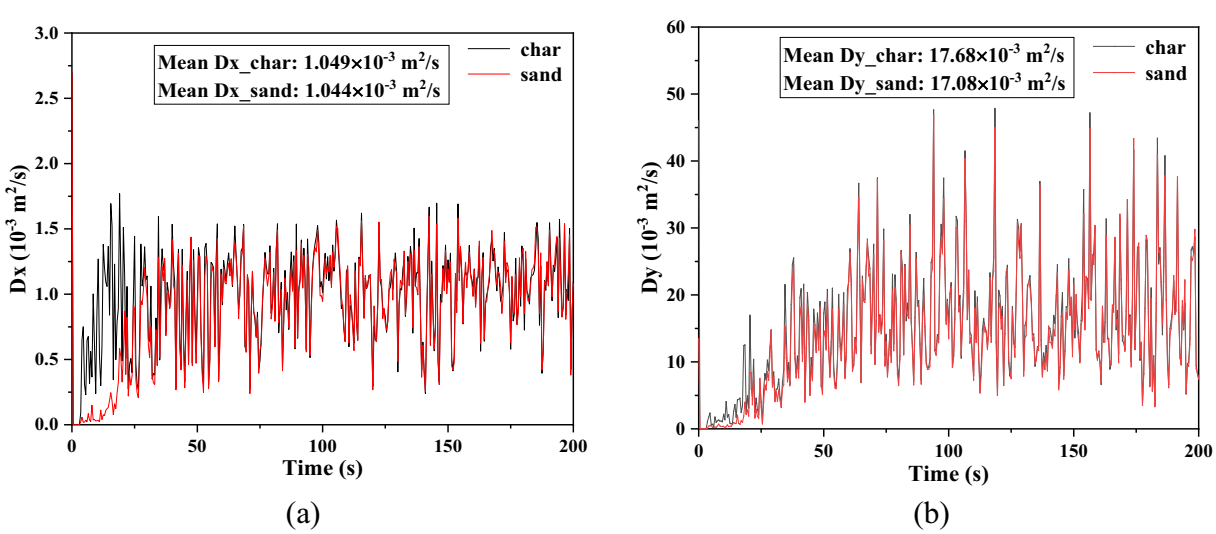

Fig. 8. Time-evolution profiles of solid horizontal dispersion coefficient (Dx) and solid axial dispersion coefficient (Dy) in the bed, U_0 = 3.0 m/s, T_b = 1073 K.

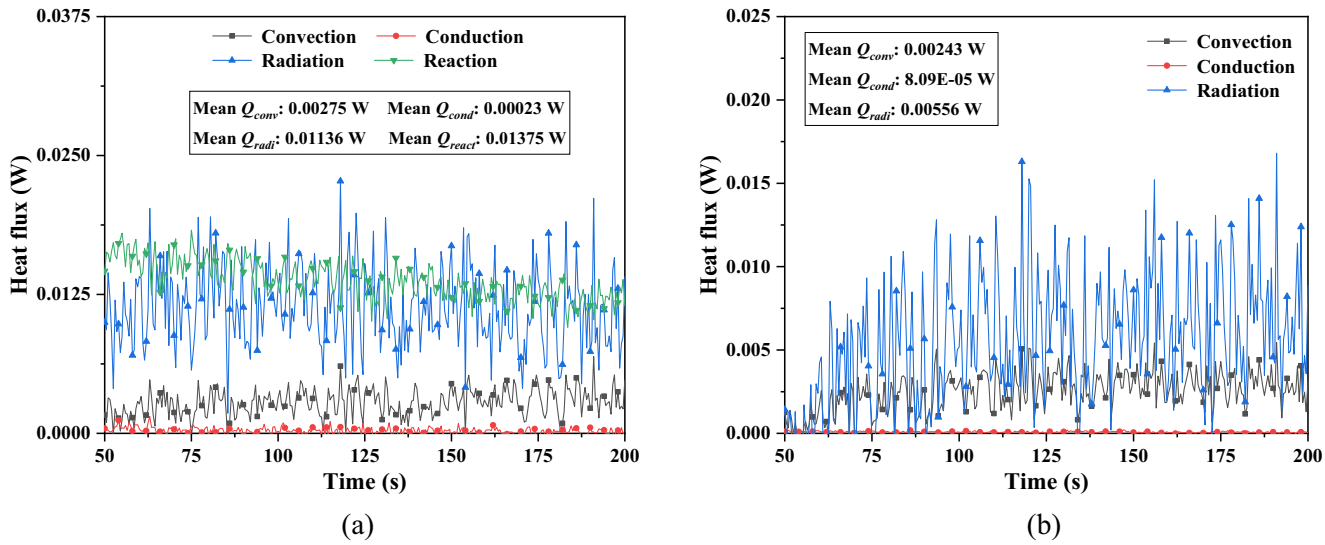

Fig. 9. Contributions of different heat transfer modes of char (a) and sand species (b), U_0 = 3.0 m/s, T_b = 1073 K.

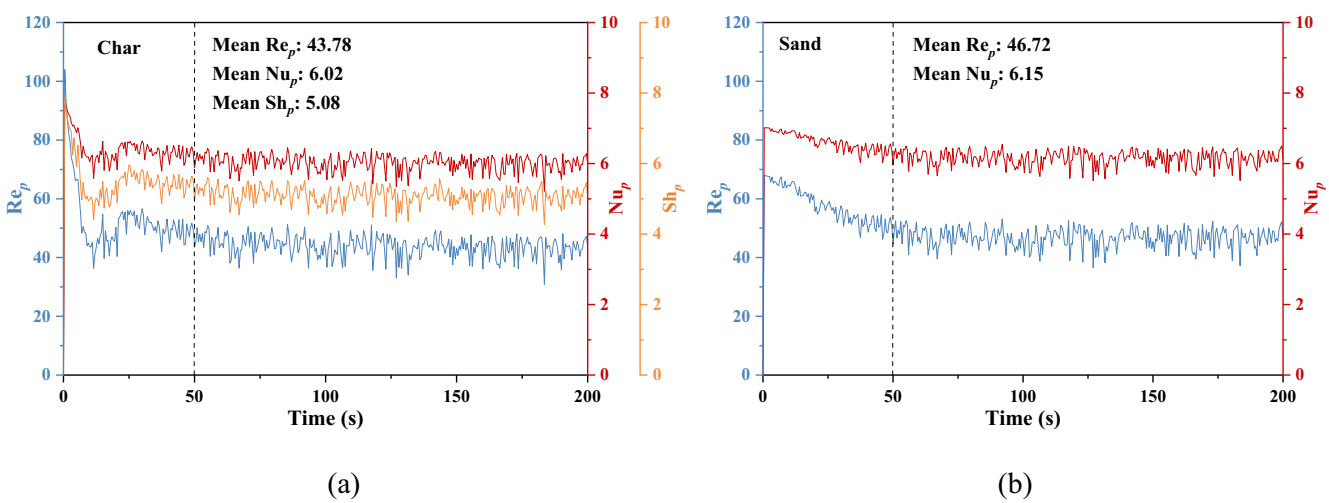

Fig. 10. Time-evolution profiles of dimensionless number (Re_p, Nu_p, Sh_p) for different particle species in the bed, U_0 = 3.0 m/s, T_b = 1073 K: (a) char; (b) sand.

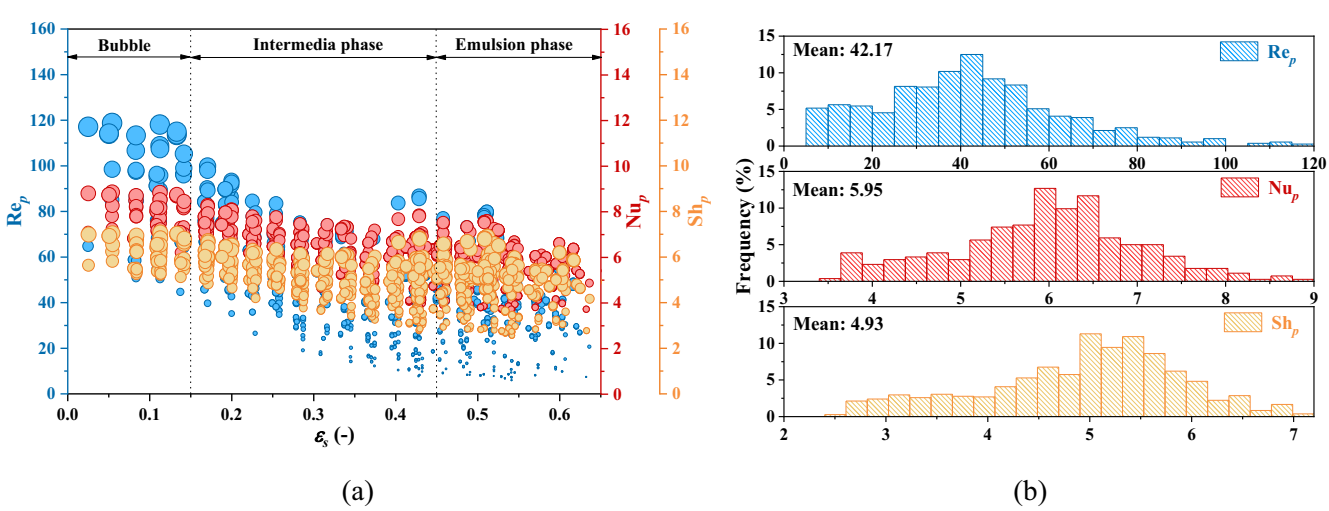

Fig. 11. (a) Relationship between char properties (Re_p is labelled by blue color; Nu_p is labelled by red color; Sh_p is labelled by yellow color; the size of scatter points represents the magnitude of slip velocity) with particle concentration (ε_s); (b) frequency of Re_p, Nu_p, and Sh_p of the char at t = 100 s. (For interpretation of the references to color in this figure legend, the reader is referred to the web version of this article.)

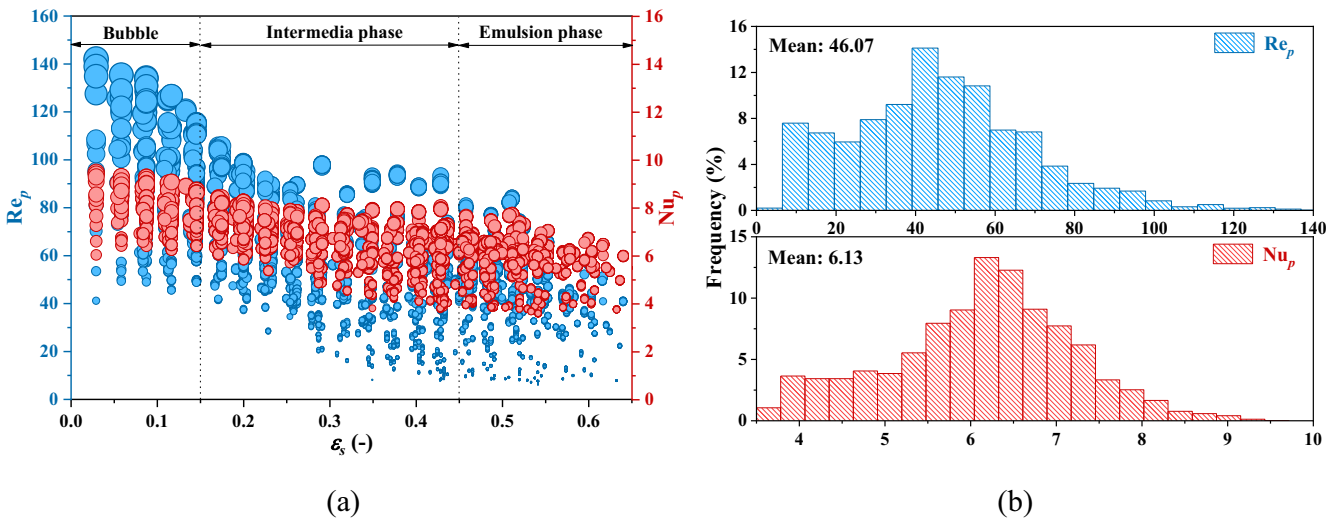

Fig. 12. (a) Relationship between sand properties (Re_p, Nu_p) with particle concentration; (b) frequency of Re_p and Nu_p of the sand at t = 100 s.

of dimensionless number for char and sand particles in the system. Similar trends of Re_p, Nu_p, and Sh_p profiles for both particle species can be observed. After the system reaches an equilibrium state, the particle-averaged dimensionless numbers are respectively 43.78, 6.02, and 5.08 for the char particle while 46.72 and 6.15 for the sand particle. A larger particle-to-gas density ratio for the sand material leads to the larger particle inertia and the resulting larger particle-gas slip velocity. Thus, the sand Re_p is larger than the char Re_p. As a result, the sand Nu_p is larger than the char Nu_p as the Nusselt number is proportional to the Reynolds number.

Fig. 11(a) shows the distributions of the dimensionless number as a function of particle concentration and slip velocity. The size of scatter points represents the magnitude of the slip velocity. Three distinct regimes can be identified by the threshold particle concentration of 0.15 and 0.45, i.e., bubble phase with a low particle concentration and high slip velocity, intermedia phase with a medium particle concentration and slip velocity, and emulsion phase with a high particle concentration and low slip velocity. Specifically, particles in the bubble have high slip velocities due to the dominant role of the interphase drag force, while particles in the emulsion phase have small slip velocities due to the significant role of the inter-particle collision force. Thus, these typical flow regimes significantly influence gas-solid momentum exchanges as distinct Re_p in three different regimes can be observed. Due to the non-linear correlation of Nu_p and Sh_p with the Re_p, the Nu_p and Sh_p show a gentle decrease with the increase of particle concentration. In other words, char particles in three distinct regimes perform a slight influence on the heat and mass transfer behaviours but a significant impact on the gas-solid momentum exchange. However, enhancing gas-solid momentum exchange still positively affects the heat and mass transfer performance. Fig. 11(b) illustrates the frequency distributions of Re_p, Nu_p, and Sh_p. Small and medium Re_p respectively in the emulsion and intermedia phases occupy the larger proportion while large Re_p in the bubble phase occupies the smaller proportion. Nu_p shows a similar frequency distribution with the Sh_p that a peak value larger than 10% can be observed.

The Re_p and Nu_p distributions for the sand material (Fig. 12) have the same trends as that for the char material. Sand particles in the bubble phase have the largest Re_p, followed by them in the intermedia phase and emulsion phase. The particle concentration shows a weak influence on sand Nu_p as it gently decreases with particle concentration. Enhancing gas-solid momentum exchange helps improve the heat and mass transfer performance. The particle averaged Re_p and Nu_p at 100 s are respectively 46.07 and 6.13.

5. Conclusion

In this work, the heat and mass transfer behaviours of char combustion in a quasi-3D BFB reactor are numerically simulated using a CFD-DEM approach with the polydispersity effect and thermochemical sub-models integrated. After model validation with experimental data regarding the mixing index, particle temperature, and particle diameter, each heat transfer mode's contribution and the particle-scale information for char and sand material are comprehensively explored. Conclusions are drawn as follows:

(a) The polydisperse drag model has to be used to reproduce bed hydrodynamics accurately when simulating a BFB system within polydisperse particles. Bubble evolution drives the chaotic motions of char and sand particles. The gaseous species generated from heterogenous (R2) and homogenous reactions (R2) intensify the bubble dynamics and the mixing of char and sand particles. A lower-temperature zone in the bottom corner of the bed can be observed due to the convective heat transfer between low-temperature inlet gas and high-temperature bed material. The mean axial position of the char tracer is larger than that of the sand tracer due to the size- and density-induced segregation mechanism.

(b) The dead zone formed in the bottom corner of the bed due to the segregation mechanism and bubble entrainment effect suppresses the ideal mixing state. Increasing gas inlet velocity performs a minor influence on the final mixing state. The axial dispersion coefficient is over one order of magnitude larger than the horizontal one, demonstrating the dominant role of the introduced gas flow in determining the bed hydrodynamics.

(c) Under the simulation conditions, the particle-averaged heat fluxes to char particles through convection, conduction, radiation, and char reaction take 9.79%, 0.82%, 40.44%, and 48.95%, respectively; the particle-averaged heat fluxes to sands through convection, conduction, and radiation take 30.28%, 1.0%, and 68.72%, respectively. For reactive char particles, the radiation and heat of reaction are dominated; for

inert sand particles, the radiation and convection are dominated. For each particle species, the conductive heat transfer is negligible in the simulation.

(d) Sand Re_p is larger than the char Re_p due to the larger particle-to-gas density ratio for the sand material and the resulting larger particle-gas slip velocity. Sand particles in the bubble phase have the largest Re_p, followed by them in the intermedia phase and emulsion phase. The particle concentration shows a weak influence on Nu_p and Sh_p as they gently decrease with particle concentration. Enhancing gas-solid momentum exchange improves the heat and mass transfer performance.

This model provides a high-fidelity tool to unveil the multi-physics characteristics of gas-solid reacting flow during the thermochemical conversion of solid fuel in fluidised bed reactors.

CRediT authorship contribution statement

Shuai Wang: Methodology, Investigation, Data curation, Formal analysis, Validation, Software, Writing - original draft. **Yansong Shen:** Conceptualization, Resources, Supervision, Project administration, Funding acquisition, Methodology, Investigation, Data curation, Formal analysis, Writing - review & editing.

Declaration of Competing Interest

The authors declare that they have no known competing financial interests or personal relationships that could have appeared to influence the work reported in this paper.

Acknowledgements

Financial support from the Australian Research Council (DP180101232 and FT190100361) is acknowledged. Computational support from National Computational Infrastructure (NCI) in Australia is also acknowledged.

References

Azmir, J., Hou, Q., Yu, A., 2019. CFD-DEM simulation of drying of food grains with particle shrinkage. Powder Technol. 343, 792–802.
Bai, Y., Si, H., 2020. Experimental study on fluidization, mixing and separation characteristics of binary mixtures of particles in a cold fluidized bed for biomass fast pyrolysis. Chem. Eng. Process. - Process Intensif. 153, 107936.
Baniasadi, M., Peters, B., Pierret, J., Vanderheyden, B., Ansseau, O., 2018. Experimental and numerical investigation into the softening Behavior of a packed bed of iron ore pellets. Powder Technol. 339, 863–871.
Batchelor, G.K., O'Brien, R.W., 1977. Thermal or electrical conduction through a granular material. Proc. R. Soc. London. A Math. Phys. Sci. 355 (1682), 313–333.
Beetham, S., Capecelatro, J., 2019. Biomass pyrolysis in fully-developed turbulent riser flow. Renew. Energ. 140, 751–760.
Beetstra, R., van der Hoef, M.A., Kuipers, J.A.M., 2007. Numerical study of segregation using a new drag force correlation for polydisperse systems derived from lattice-Boltzmann simulations. Chem. Eng. Sci. 62 (1–2), 246–255.
Bird, R.B., 2002. Transport phenomena. Appl. Mech. Rev. 55 (1), R1–R4.
Botterill, J.S.M., 1975. Fluid-bed heat transfer. Gas-fluidized bed behaviour and its influence on bed thermal properties.
Breault, R.W., 2006. A review of gas–solid dispersion and mass transfer coefficient correlations in circulating fluidized beds. Powder Technol. 163 (1–2), 9–17.
British, C.U.R.A., Field, M.A., 1967. Combustion of pulverised coal. BcURA Leatherhead.
Bu, C. et al., 2015. Devolatilization of a single fuel particle in a fluidized bed under oxy-combustion conditions Part A: Experimental results. Combust. Flame 162 (3), 797–808.
Burcat, A., Ruscic, B., 2005. Third millenium ideal gas and condensed phase thermochemical database for combustion (with update from active thermochemical tables). Argonne National Lab.(ANL), Argonne, IL (United States).
Clarke, D.A., Sederman, A.J., Gladden, L.F., Holland, D.J., 2018. Investigation of Void Fraction Schemes for Use with CFD-DEM Simulations of Fluidized Beds. Ind. Eng. Chem. Res. 57 (8), 3002–3013.
Cluet, B., Mauviel, G., Rogaume, Y., Authier, O., Delebarre, A., 2015. Segregation of wood particles in a bubbling fluidized bed. Fuel Process. Technol. 133, 80–88.
Cui, J., Hou, Q., Shen, Y., 2020. CFD-DEM study of coke combustion in the raceway cavity of an ironmaking blast furnace. Powder Technol. 362, 539–549.
Cundall, P.A., Strack, O.D., 1979. A discrete numerical model for granular assemblies. Geotechnique 29 (1), 47–65.
DeSai, P.R., Wen, C., Bissett, L.A., 1978. Computer Modeling of the Morgantown Energy Research Center's Fixed Bed Gasifier. US Department of Energy, Technical Information Center.
Dryer, F.L., Glassman, I., 1973. High-temperature oxidation of CO and CH4. Elsevier, pp. 987–1003.
Ergun, S., Orning, A.A., 1949. Fluid flow through randomly packed columns and fluidized beds. Ind. Eng. Chem. 41 (6), 1179–1184.
Ferziger, J.H., Peric, M., 2012. Computational methods for fluid dynamics. Springer Science & Business Media.
Garg, R., Galvin, J., Li, T., Pannala, S., 2012. Open-source MFIX-DEM software for gas–solids flows: Part I—Verification studies. Powder Technol. 220, 122–137.
Geng, Y., Che, D., 2011. An extended DEM–CFD model for char combustion in a bubbling fluidized bed combustor of inert sand. Chem. Eng. Sci. 66 (2), 207–219.
Gidaspow, D., 1994. Multiphase flow and fluidization: continuum and kinetic theory descriptions. Academic press.
Hayhurst, A.N., Parmar, M.S., 1998. Does solid carbon burn in oxygen to give the gaseous intermediate CO or produce CO2 directly? Some experiments in a hot bed of sand fluidized by air. Chem. Eng. Sci. 53 (3), 427–438.
Hayhurst, A.N., Parmar, M.S., 2002. Measurement of the mass transfer coefficient and Sherwood number for carbon spheres burning in a bubbling fluidized bed. Combust. Flame 130 (4), 361–375.
Hill, R.J., Koch, D.L., Ladd, A.J., 2001. Moderate-Reynolds-number flows in ordered and random arrays of spheres. J. Fluid Mech. 448, 243–278.
Hobbs, M.L., Radulovic, P.T., Smoot, D.L., 1993. Combustion and gasification of coals in fixed-beds. Prog. Energ. Combust. 19 (6), 505–586.
Hou, Q.F., Zhou, Z.Y., Yu, A.B., 2012. Computational study of heat transfer in a bubbling fluidized bed with a horizontal tube. AIChE J. 58 (5), 1422–1434.
Jiang, Z., Hagemeier, T., Bück, A., Tsotsas, E., 2018. Color-PTV measurement and CFD-DEM simulation of the dynamics of poly-disperse particle systems in a pseudo-2D fluidized bed. Chem. Eng. Sci. 179, 115–132.
Kinaci, M.E., Lichtenegger, T., Schneiderbauer, S., 2020. A CFD-DEM model for the simulation of direct reduction of iron-ore in fluidized beds. Chem. Eng. Sci. 227, 115858.
Ku, X., Li, T., Løvås, T., 2015. CFD–DEM simulation of biomass gasification with steam in a fluidized bed reactor. Chem. Eng. Sci. 122, 270–283.
Kunii, D., Levenspiel, O., 2013. Fluidization engineering. Elsevier.
La Nauze, R.D., Jung, K., Kastl, J., 1984. Mass transfer to large particles in fluidised beds of smaller particles. Chem. Eng. Sci. 39 (11), 1623–1633.
Lacey, P.M.C., 1954. Developments in the theory of particle mixing. J. Appl. Chem. (London) 4 (5), 257–268.
Liu, D., Chen, X., 2010. Lateral solids dispersion coefficient in large-scale fluidized beds. Combust. Flame 157 (11), 2116–2124.
Liu, D., Chen, X., 2011. Experimental profiles of lateral mixing of feed particles in a three-dimensional fluidized bed. AIChE J. 57 (6), 1459–1469.
Liu, D., Chen, X., Zhou, W., Zhao, C., 2011. Simulation of char and propane combustion in a fluidized bed by extending DEM–CFD approach. P. Combust. Inst. 33 (2), 2701–2708.
Lu, L., Morris, A., Li, T., Benyahia, S., 2017. Extension of a coarse grained particle method to simulate heat transfer in fluidized beds. Int. J. Heat Mass Tran. 111, 723–735.
Medrano, J.A., Gallucci, F., Boccia, F., Alfano, N., van Sint Annaland, M., 2017. Determination of the bubble-to-emulsion phase mass transfer coefficient in gas-solid fluidized beds using a non-invasive infra-red technique. Chem. Eng. J. 325, 404–414.
Mohseni, M., Peters, B., 2016. Effects of particle size distribution on drying characteristics in a drum by XDEM: A case study. Chem. Eng. Sci. 152, 689–698.
Musser, J.M., 2011. Modeling of Heat Transfer and Reactive Chemistry for Particles in Gas-Solid Flow Utilizing Continuum-Discrete Methodology (CDM). West Virginia University Libraries.
Ostermeier, P., Fischer, F., Fendt, S., DeYoung, S., Spliethoff, H., 2019. Coarse-grained CFD-DEM simulation of biomass gasification in a fluidized bed reactor. Fuel 255, 115790.
Park, H.C., Choi, H.S., 2013. The segregation characteristics of char in a fluidized bed with varying column shapes. Powder Technol. 246, 561–571.
Peters, B., Hoffmann, F., 2016. Iron ore reduction predicted by a discrete approach. Chem. Eng. J. 304, 692–702.
Sánchez-Prieto, J., Hernández-Jiménez, F., Garcia-Gutierrez, L.M., Soria-Verdugo, A., 2017. Experimental study on the characteristic mixing time of solids and its link with the lateral dispersion coefficient in bubbling fluidized beds. Chem. Eng. J. 307, 113–121.
Shen, Y, Guo, B, Chew, S, Austin, P, Yu, A, 2016. Modeling of Internal State and Performance of an Ironmaking Blast Furnace: Slot *vs*Sector Geometries. Metallurgical and Materials Transactions B 47 (2), 1052–1062.
Shen, Y, Shiozawa, T, Austin, P, Yu, A, 2014. Model study of the effect of bird's nest on transport phenomena in the raceway of an ironmaking blast furnace. Minerals Engineering 63, 91–99.
Shen, Y, Yu, A, 2016. Modelling of injecting a ternary coal blend into a model ironmaking blast furnace. Minerals Engineering 90, 89–95.

Shimura, K., Matsuo, A., 2019. Using an extended CFD–DEM for the two-dimensional simulation of shock-induced layered coal-dust combustion in a narrow channel. P. Combust. Inst. 37 (3), 3677–3684.
Syamlal, M., Bissett, L.A., 1992. METC gasifier advanced simulation (MGAS) model. USDOE Morgantown Energy Technology Center, WV (United States).
Tang, T., He, Y., Tai, T., Wen, D., 2017. DEM numerical investigation of wet particle flow behaviors in multiple-spout fluidized beds. Chem. Eng. Sci. 172, 79–99.
Tsuji, Y., Kawaguchi, T., Tanaka, T., 1993. Discrete particle simulation of two-dimensional fluidized bed. Powder Technol. 77 (1), 79–87.
Wakao, N., Kagei, S., 1982. Heat and mass transfer in packed beds, 1. Taylor & Francis.
Wang, J., 2020. Continuum theory for dense gas-solid flow: A state-of-the-art review. Chem. Eng. Sci. 215, 115428.
Wang, Q. et al., 2015. Numerical study of particle segregation in a coal beneficiation fluidized bed by a TFM–DEM hybrid model: Influence of coal particle size and density. Chem. Eng. J. 260, 240–257.
Wang, S., Luo, K., Fan, J., 2020. CFD-DEM coupled with thermochemical sub-models for biomass gasification: Validation and sensitivity analysis. Chem. Eng. Sci. 217, 115550.
Wang, S., Luo, K., Hu, C., Lin, J., Fan, J., 2019. CFD-DEM simulation of heat transfer in fluidized beds: Model verification, validation, and application. Chem. Eng. Sci. 197, 280–295.
Wang, S., Luo, K., Yang, S., Hu, C., Fan, J., 2017. Parallel LES-DEM simulation of dense flows in fluidized beds. Appl. Therm. Eng. 111, 1523–1535.
Wang, S., Shen, Y., 2020. CFD-DEM study of biomass gasification in a fluidized bed reactor: Effects of key operating parameters. Renew. Energ. 159, 1146–1164.
Wen, C.Y., 1966. Mechanics of fluidization, pp. 100-111.
Wen, C.Y., Chen, H., Onozaki, M., 1982. User's manual for computer simulation and design of the moving-bed coal gasifier. Final report. West Virginia Univ., Morgantown (USA). Dept. of Chemical Engineering.
Yang, S., Luo, K., Fang, M., Fan, J., Cen, K., 2014. Discrete Element Study of Solid Mixing Behavior with Temperature Difference in Three-Dimensional Bubbling Fluidized Bed. Ind. Eng. Chem. Res. 53 (17), 7043–7055.
Yang, S., Zhou, T., Wei, Y., Hu, J., Wang, H., 2019. Influence of size-induced segregation on the biomass gasification in bubbling fluidized bed with continuous lognormal particle size distribution. Energ. Convers. Manage. 198, 111848.
Yang, W.J., Zhou, Z.Y., Yu, A.B., Pinson, D., 2015. Particle scale simulation of softening–melting behaviour of multiple layers of particles in a blast furnace cohesive zone. Powder Technol. 279, 134–145.
Yoon, H., Wei, J., Denn, M.M., 1978. A model for moving-bed coal gasification reactors. AIChE J. 24 (5), 885–903.
Yue, Y., Wang, T., Sakai, M., Shen, Y., 2019. Particle-scale study of spout deflection in a flat-bottomed spout fluidized bed. Chem. Eng. Sci. 205, 121–133.
Zhang, K., Wang, S., Li, B., He, Y., Zhao, Y., 2020. Heat transfer in a pulsed fluidized bed by using coupled CFD-DEM method. Powder Technol. 367, 497–505.
Zhao, Y., Jiang, M., Liu, Y., Zheng, J., 2009. Particle-scale simulation of the flow and heat transfer behaviors in fluidized bed with immersed tube. AIChE J. 55 (12), 3109–3124.
Zhong, W., Yu, A., Zhou, G., Xie, J., Zhang, H., 2016. CFD simulation of dense particulate reaction system: Approaches, recent advances and applications. Chem. Eng. Sci. 140, 16–43.
Zhou, H., Flamant, G., Gauthier, D., 2004a. DEM-LES of coal combustion in a bubbling fluidized bed. Part I: gas-particle turbulent flow structure. Chem. Eng. Sci. 59 (20), 4193–4203.
Zhou, H., Flamant, G., Gauthier, D., 2004b. DEM-LES simulation of coal combustion in a bubbling fluidized bed Part II: coal combustion at the particle level. Chem. Eng. Sci. 59 (20), 4205–4215.
Zhou, Z.Y., Yu, A.B., Zulli, P., 2009. Particle scale study of heat transfer in packed and bubbling fluidized beds. AIChE J. 55 (4), 868–884.
Zhu, H.P., Zhou, Z.Y., Yang, R.Y., Yu, A.B., 2007. Discrete particle simulation of particulate systems: Theoretical developments. Chem. Eng. Sci. 62 (13), 3378–3396.
Zhu, H.P., Zhou, Z.Y., Yang, R.Y., Yu, A.B., 2008. Discrete particle simulation of particulate systems: A review of major applications and findings. Chem. Eng. Sci. 63 (23), 5728–5770.